Miner Petrol (2009) 95:135–157
DOI 10.1007/s00710-008-0026-1

ORIGINAL PAPER

Contrasting fluid evolution of granulite-facies marbles: implications for a high-T intermediate-P terrain in the Famatinian Range, San-Juan, Argentina

Florian Gallien · Aberra Mogessie · Ernesto Bjerg · Sergio Delpino · Brigida Castro de Machuca

Received: 16 July 2008 / Accepted: 23 September 2008 / Published online: 17 October 2008

Abstract High-temperature, intermediate-pressure calc-silicate marbles occur in the granulite-facies terrain of the La Huerta Range in the Province of San Juan, NW-Argentina, in three bulk-compositional varieties: Type (1) dolomite-absent scapolite-wollastonite-grandite-clinopyroxene-quartz—calcite marbles; Type (2) diopside-forsterite-spinel-corundum—calcite marbles with dolomite exolution lamellae in calcite; Type (3) serpentinized forsterite-spinel-dolomite marbles. An isobaric cooling path from peak-metamorphic conditions of 860°C to 750°C at 6.5 kbar is inferred from scapolite-wollastonite-grandite reaction textures in Type (1) and is consistent with cooling after an advective heat input from related gabbroic and tonalitic intrusive bodies. Stable carbon and oxygen isotope geochemistry was used to decipher the fluid/rock evolution of the three marble types. An interpreted four-stage temperature-time-fluid flow path comprises: (1) infiltration of pre-peak-metamorphic fluids, depleted in $\delta^{18}O$, that caused a shift of primary sedimentary $\delta^{18}O$ ratios to lower values (19.6–20.0); (2) syn-metamorphic fluid liberation from Type (1) marbles with evidence for processes close to batch devolatilization that caused a weak coupled ^{13}C and ^{18}O depletion during prograde metamorphism. A different devolatilization behaviour, close to Rayleigh fractionation, texturally associated with fold settings indicates that granulite-facies fluid flow was focused rather than pervasive; (3) H_2O-absent conditions were dominant when coronal grandite formed during incipient high-temperature isobaric cooling at the expense of scapolite and wollastonite in the Type (1) marbles; (4) intense post-peak- hydration of Type (2) and Type (3) marbles is the last recognizable metasomatic event. In combination, the three marble types record fluid infiltration both before and after the metamorphic peak.

Editorial handling: R. Abart

F. Gallien (✉) · A. Mogessie
Institut für Erdwissenschaften,
Bereich Mineralogie und Petrologie, Karl-Franzens-Universität,
Graz, Universitätsplatz 2,
8010 Graz, Austria
e-mail: gallienf@stud.uni-graz.at

E. Bjerg · S. Delpino
CONICET-Department of Geology, Universidad Nacional del Sur,
Bahia Blanca, Argentina

B. Castro de Machuca
CONICET-Institute of Geology,
Universidad Nacional de San Juan,
San Juan, Argentina

Introduction

The Valle Fértil-La Huerta ranges (Fig. 1a,b) in San Juan Province, NW Argentina belong to the Famatinian orogen in the Western Sierras Pampeanas which are considered to be the "key" for understanding the relation between the Pampean and Laurentian derived terranes at the western margin of Gondwana (Ramos et al. 1996; Thomas and Astini 1996; Pankhurst et al. 1998). Within the Valle Fèrtil-La Huerta Range regional scale I-type granitoids and gabbroic bodies intruded a premetamorphic basement of amphibolite facies metasediments (Caminos 1979; Toselli et al. 1996; Saavedra et al. 1998; Pankhurst et al. 2000). Metacarbonate units (up to 100 m thick) of the La Huerta Range are enclosed within the high grade metamorphosed granulite-gneisses, migmatites and amphibolites and represent a heterogeneous sequence of layered impure dolomite and calcite marbles. Age data from the magmatic units and

migmatites from Valle Fèrtil-La Huerta are coeval and range between 500 Ma and 460 Ma (Pontoriero and Castro de Machuca 1999; Pankhurst et al. 1998, 2000). Thus the magmatic activity in Valle Fértil and La Huerta Ranges is considered to be the heat source for the granulite facies conditions which has affected all rock types in the area.

Granulite-facies calc-silicate rocks have been frequently reported from India (e.g. Bhowmik et al. 1995; Shaw and Arima 1996; Sengupta et al. 1997; Satish-Kumar and Harley 1998). Mathavan and Fernando (2001) describe evidence for isobaric cooling in grossular-wollastonite-scapolite calc-silicate rocks from Sri Lanka. Scapolite-wollastonite calc-silicate granulites from East Antarctica have been studied by Motoyoshi et al. (1991), Harley and Buick (1992) and Fitzsimons and Harley (1994). Corona textures can help determining the P-T-fluid history of rocks under granulite-facies conditions. Grandite (grossular-andradite solid-solution) corona textures in calc-silicate granulites have been the focus of the studies of Dasgupta and Pal (2005). Calc-silicate coronas around hornblendite xenoliths in granulite facies marbles from the Ivrea zone have been reported by Abart et al. (2001) and Abart and Sperb (2001). A series of granulite-facies rocks, including metacarbonates, from the lower crust in Southern Italy have been reported by Schenk (1983).

The reactive behaviour of calc-silicate rocks and impure dolomitic marbles during metamorphism makes them very suitable monitors of the fluid-rock evolution during metamorphism. The buffering of fluid composition during devolatilization reactions has become an important petrogenetic parameter to evaluate the fluid-rock evolution during metamorphism (Greenwood 1967, 1975). The case of an "internally buffered" fluid evolution, with the fluid in local equilibrium with the solids along a P and/or T gradient, is guaranteed if the rock's permeability is negligible and the fluids liberated during devolatilization can not escape from the reaction site, thus no fluid leaves or enters. However, if the rock experienced significant infiltration of an externally derived, generally H_2O-rich fluid, out of equilibrium with the host (e.g. contact metamorphic events), the fluid evolving during devolatilization reactions becomes successively diluted ("externally buffered") (Ferry 1991).

The granulite-facies terrain of the Valle Fértil, La Huerta Ranges, have been interpreted as an advectively heated area recording high-T metamorphism at intermediate P (i.e. regional contact metamorphism-by Pankhurst et al. 2000 and Rossi et al. 2002).

The present study focuses on calc-silicate reaction textures and stable C-O isotope signatures to better constrain the P-T-t-fluid history of the La Huerta Range. This is the first time that such a detailed study has been made on these rocks from the La Huerta Range.

Geological setting

The Valle Fértil-La Huerta Ranges (Fig. 1a,b), located about 130 km NE of San Juan City in the Province of San Juan, NW-Argentina are part of the Western Sierras Pampeanas tectono-stratigraphical province. They are composed of a suite of granulite-facies paragneisses and migmatites with subordinate interlayered carbonates (Caminos 1979), which were discordantly intruded by several large magmatic bodies during the Famatinian magmatic cycle. The Late Cambrian and Early Ordovician (500–460 Ma) subduction-related Famatinian magmatic arc developed on the overriding plate when an allochtonous Laurentia-derived terrain approached the western margin of Gondwana (Ramos et al. 1996; Thomas and Astini 1996; Toselli et al. 1996; Pankhurst et al. 1998; Otamendi et al. 2007). The paleogeographic location of the Famatinian magmatic arc is interpreted by several authors as an outer magmatic arc (Rapela et al. 1992) located close to the southwestern margin of Gondwana in the Iapetus Ocean (Dalziel et al. 1994). The associated magmatic suite comprises tonalitic granodiorites, granites, gabbros to gabbronorites and pegmatites (Castro de Machuca 1990; Castro de Machuca et al. 1995; Toselli et al. 1996; Pontoriero and Castro de Machuca 1999; Mogessie et al. 2007 and references therein). Within the paragneiss sequence of the southern La Huerta Range, metre- to hundred metre-thick impure calcite marbles occur, interlayered with dolomitic marbles. The coarse-grained calcite and dolomitic marbles are white to pale yellow and contain darker centimetre to decimetre thick silicate-rich layers. In some outcrops intensely folded calc-silicate layers appear as ripple structures on the weathering surface. Typical granulite-facies calc-silicate parageneses comprising wollastonite, scapolite, grandite and clinopyroxene developed in the impure calcite marbles (Type 1), whereas forsterite, spinel and clinopyroxene were formed in the dolomitic marbles (Type 2). The siliceous dolomite marbles (Type 3) form strongly weathered brownish-yellow layers that contain retrograde talc, brucite, amphibole, serpentine, chlorite and relict forsterite + spinel. Centimetre-wide metasomatic pink to white coarse-grained calcite domains occur along the gneiss-marble- and gabbro-marble contacts. Peak temperature conditions of ~800°C are reported by Delpino et al. (2008) and Otamendi et al. (2007) from metasedimentary migmatitic gneisses in the Valle Fertil Range, about 60 km north of La Huerta Range.

Methods

The chemical compositions of minerals were determined using a Jeol SEM 6310 scanning electron microscope using EDS and WDS systems. Routine analyses were done for the

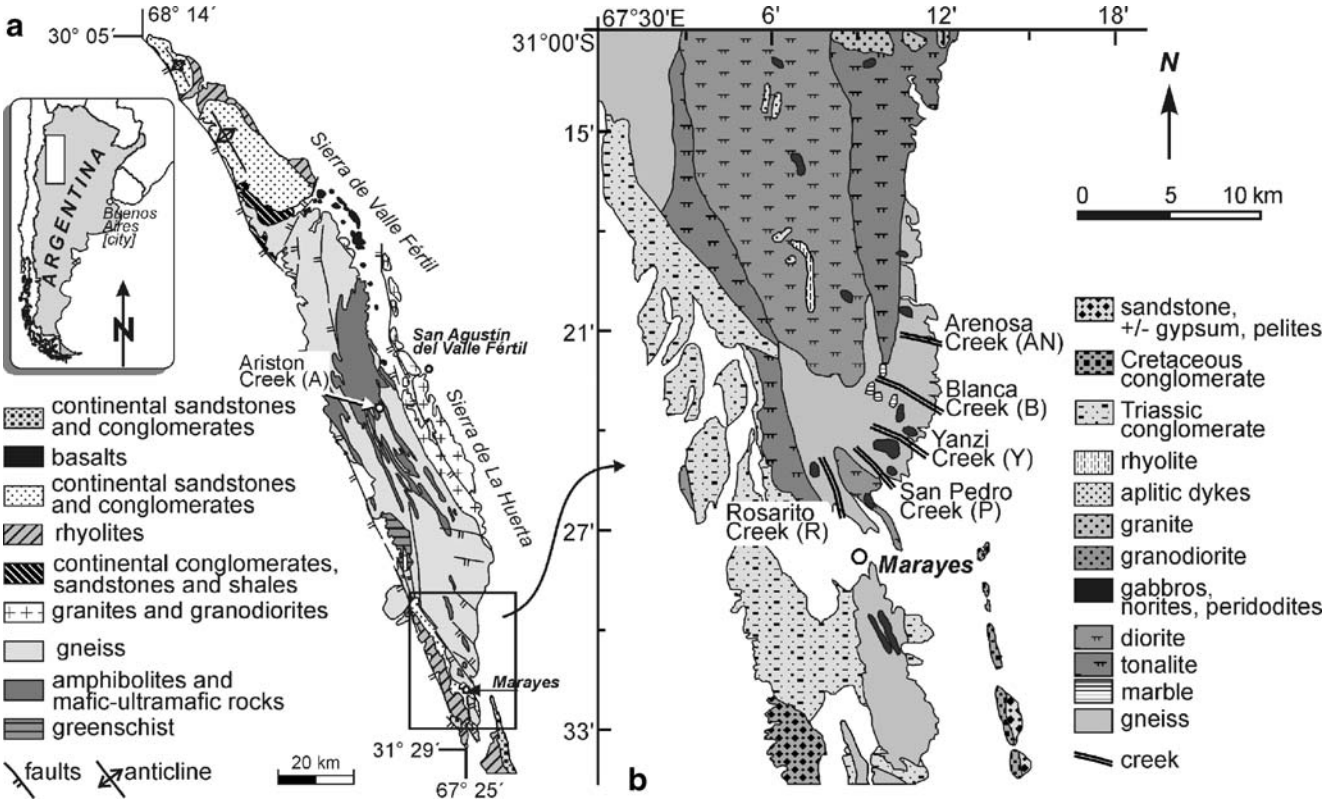

Fig. 1 **a** Simplified geological map of the Valle Fértil-La Huerta Ranges, modified after Ragona et al. (1995). The area of detailed study in the south of La Huerta Range is indicated by the box; **b** Geological map of the southern part of La Huerta Range modified after Vujovich et al. (2000). The simplified geological map shows the main lithologies in the sampling areas: Arenosa Creek, Blanca Creek, Yanzi Creek, San Pedro Creek and Rosarito Creek. Individual marble outcrops are too small to be shown at this scale

elements (with standards): F (F-phlogopite); Na (albite); Mg and Fe (garnet); Al, K and Si (adularia); S (barite); Cl (atacamite), Ca and Ti (titanite); Cr (chromite); Mn (rhodonite); Zn (gahnite) and Zr (zircon). Analytical conditions were 15 kV acceleration voltage and 5 nA beam current. Beam diameter was 5 μm for silicates and 30 μm for carbonates. For bulk-rock chemical analysis a Bruker Pioneer S4 X-Ray fluorescence spectrometer was used. Samples were prepared as fused pellets using $Li_2B_4O_7$ flux. Stable isotope measurements for $\delta^{18}O$ and $\delta^{13}C$ were made on a Finnigan Mat Delta^{plus} mass spectrometer at the Karl-Franzens University of Graz and at the Joanneum Research (Graz) on a ThermoFinnigan GasBench II equipped with a CTC Combi-Pal autosampler, linked to a Delta^{plus} XP mass spectrometer. To liberate CO_2 from carbonates, samples were reacted with concentrated phosphoric acid at 70°C. Values of $\delta^{18}O$ and $\delta^{13}C$ are given relative to V-SMOW and V-PDB respectively. NBS19 was used as standard material with a typical standard deviation of 0.0386‰.

Petrography

Three different types of siliceous marbles can be distinguished: Type (1)-dolomite-free calcite marble contain scapolite, wollastonite, grandite and quartz as well as diopside as the only Mg-bearing phase. Epidote-quartz-calcite symplectites are present and have been formed at the expense of grandite. Type (2) dolomitic marbles exhibit dolomite exolution lamellae of various thickness in calcite and minor late, often coronitic dolomite from forsterite breakdown reactions but no primary dolomite. These type (2) marbles contain diopside, forsterite, spinel and corundum. Type (3) dolomitic marbles contain dolomite, forsterite, spinel, serpentine, brucite and talc. Transitions between these main types occur, as bulk chemistry may vary on a millimetre scale within pockets and layers.

Type (1): dolomite-free calcite marbles

These calc-silicate assemblages appear as fine-grained layers in the calcite matrix of 1–5 mm thickness. Based on the silicate phases present, Type (1) marbles have four subdivisions:

Type (1a): Clinopyroxene—quartz aggregates in a coarse-grained calcite matrix:

Clinopyroxene shows well-developed high-T recrystallization textures (Fig. 2a), such as triple junctions between clinopyroxene grains and rounded low-energy phase boundaries with the surrounding calcite matrix. Quartz occurs in reaction rims around clinopyroxene.

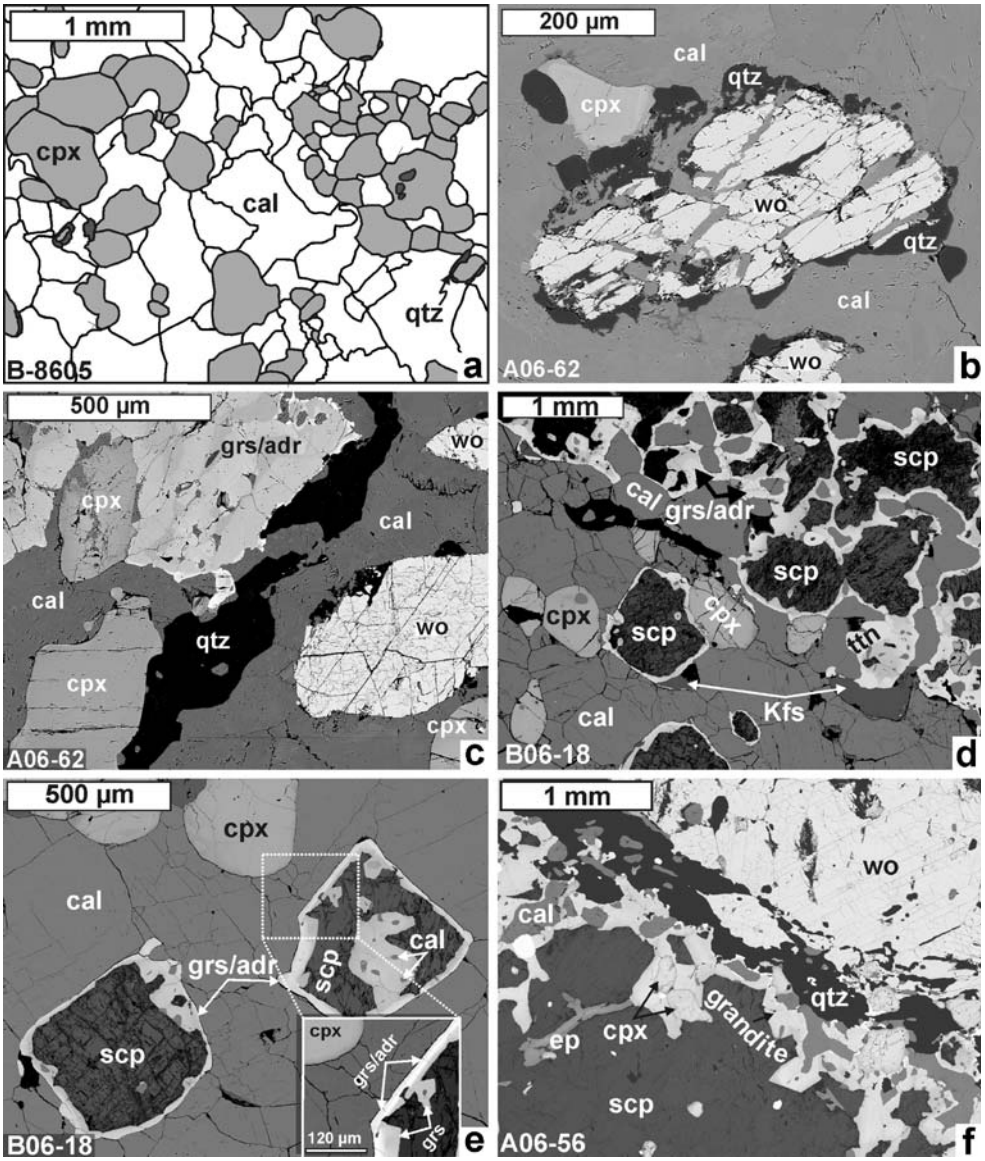

Fig. 2 Representative calc-silicate textures in Type (1) marbles. **a** The sketch shows clinopyroxene-quartz associations in a calcite matrix. Triple junctions between clinopyroxene and rounded low-energy boundaries between clinopyroxene and calcite indicate solid-state grain boundary adjustment during high-T metamorphism. **b** Large wollastonite blades in calcite decomposing to quartz + calcite. **c** Grandite-clinopyroxene-quartz assemblage with wollastonite. The patchy distribution of the andradite component in grossular is indicated by darker and brighter parts of the grandite grain. **d** Grandite reaction textures replacing scapolite in a calcite matrix. **e** Coronal grandite around scapolite. **f** Grandite-quartz reaction rim between wollastonite and scapolite. Abbreviations: (adr) andradite, (an) anorthite, (cal) calcite, (cpx) clinopyroxene, (ep) epidote, (grs) grossular, (qtz) quartz, (scp) scapolite, (ttn) titanite, (wo) wollastonite

Type (1b), Wollastonite-grandite-clinopyroxene-calcite assemblage:

In addition to wollastonite, clinopyroxene and quartz occur in variable modal proportions together with accessory grandite. Granoblastic wollastonite-clinopyroxene associations (Fig. 2b) form centimetre-wide alternating layers within coarse-grained calcite marbles. Grandite is found in aggregates with clinopyroxene within a coarse-grained wollastonite—calcite matrix (Fig. 2c). Quartz is restricted to quartz-calcite replacement textures around wollastonite (Fig. 2b), which are products of the CO2 consuming model reaction:

$$\text{wollastonite} + CO_2 = \text{quartz} + \text{calcite} \quad (1)$$

Type (1c), Scapolite-clinopyroxene-grandite-calcite assemblage:

Polygonal coarse-grained scapolite occurs together with clinopyroxene and K-feldspar in a calcite matrix. Titanite and apatite are common accessory phases. Scapolite is enveloped by grandite reaction rims. Back scattered electron images (BSE; Fig. 2d and e) show the relation between scapolite, clinopyroxene and grandite. Based on the grandite coronas around scapolite, the following end-member reaction is proposed:

$$1\,\text{scapolite} + 5\,\text{calcite} + 3\,\text{quartz} = 3\,\text{grossular} + 6\,CO_2 \quad (2)$$

Type (1d), Scapolite-wollastonite-clinopyroxene-grandite-quartz-calcite assemblage:

Grandite reaction rims of variable thickness are developed along the scapolite-wollastonite and scapolite-clinopyroxene phase boundaries (Fig. 2f). Clinopyroxene is considered to be an ubiquitous phase. Based on textural and compositional evidence, two reactions can be proposed for the

formation of grandite coronas. The possible end-member reactions are

$$1\ \text{scapolite} + 5\ \text{wollastonite} = 3\ \text{grossular} + 2\ \text{quartz} + 1\ CO_2 \quad (3)$$

$$1\ \text{scapolite} + 3\ \text{wollastonite} + 2\ \text{calcite} = 3\ \text{grossular} + 3\ CO_2 \quad (4)$$

The participation of clinopyroxene in the formation of these grandite coronas is inferred by a decreasing hedenbergite content at the immediate contact with grandite coronas (Fig. 3). Such textural relations and compositional variations were reported by Harley and Buick (1992) and Sengupta et al. (1997). The role of clinopyroxene in the grandite-forming reactions has been discussed by Warren et al. (1987), Fitzsimons and Harley (1994), Shaw and Arima (1996) and Satish-Kumar and Harley (1998), and the following reactions are likely:

$$2\ \text{wollastonite} + 4\ \text{hedenbergite} + O_2 = 2\ \text{grandite(ss)} + 4\ \text{quartz} \quad (5)$$

$$1\ \text{hedenbergite} + 1\ \text{scapolite} + 3\ \text{calcite} = 3\ \text{grandite (ss)} + CO_2 \quad (6)$$

Type (2) dolomitic marbles

The typical mineral paragenesis is forsterite, spinel, corundum, clinopyroxene, phlogopite and calcite containing dolomite exsolution lamellae of variable thickness. Baddeleyite and apatite are accessory phases. Based on detailed petrographic studies on representative samples several reaction textures have been documented:

Clinopyroxene coronas enveloping quartz (Fig. 4a) developed by the reaction:

$$2\ \text{quartz} + 1\ \text{dolomite} = 1\ \text{diopside} + 2\ CO_2 \quad (7)$$

Inclusions of coarse-grained corundum in spinel are considered to be evidence of the prograde spinel-forming decarbonation reaction (Fig. 4b):

$$1\ \text{corundum} + 1\ \text{dolomite} = 1\ \text{spinel} + 1\ \text{calcite} + 1\ CO_2 \quad (8)$$

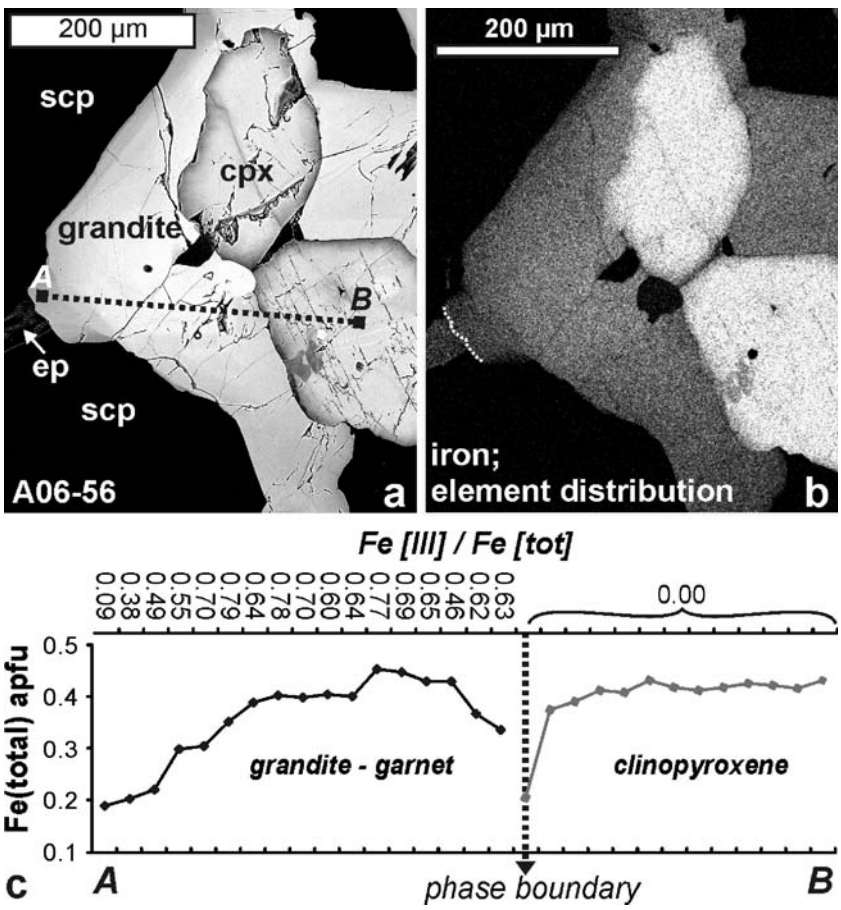

Fig. 3 **a** Type (1) calc-silicate sample; back scattered electron image of grandite formed at a scapolite-clinopyroxene interface. To demonstrate changes in the X_{Fe} content in grandite and clinopyroxene an electron microprobe profile was made along line A-B. **b** The iron distribution image shows a decrease of the iron content in the grandite with increasing distance towards the clinopyroxene. The outermost rim of the clinopyroxene grain shows a depletion in the iron content; **c** The profile along A-B shows the Fe(total) content of both phases. The Fe^{3+} / Fe[tot] in grandite is also shown. Clinopyroxene becomes successively depleted in Fe towards the grandite interface

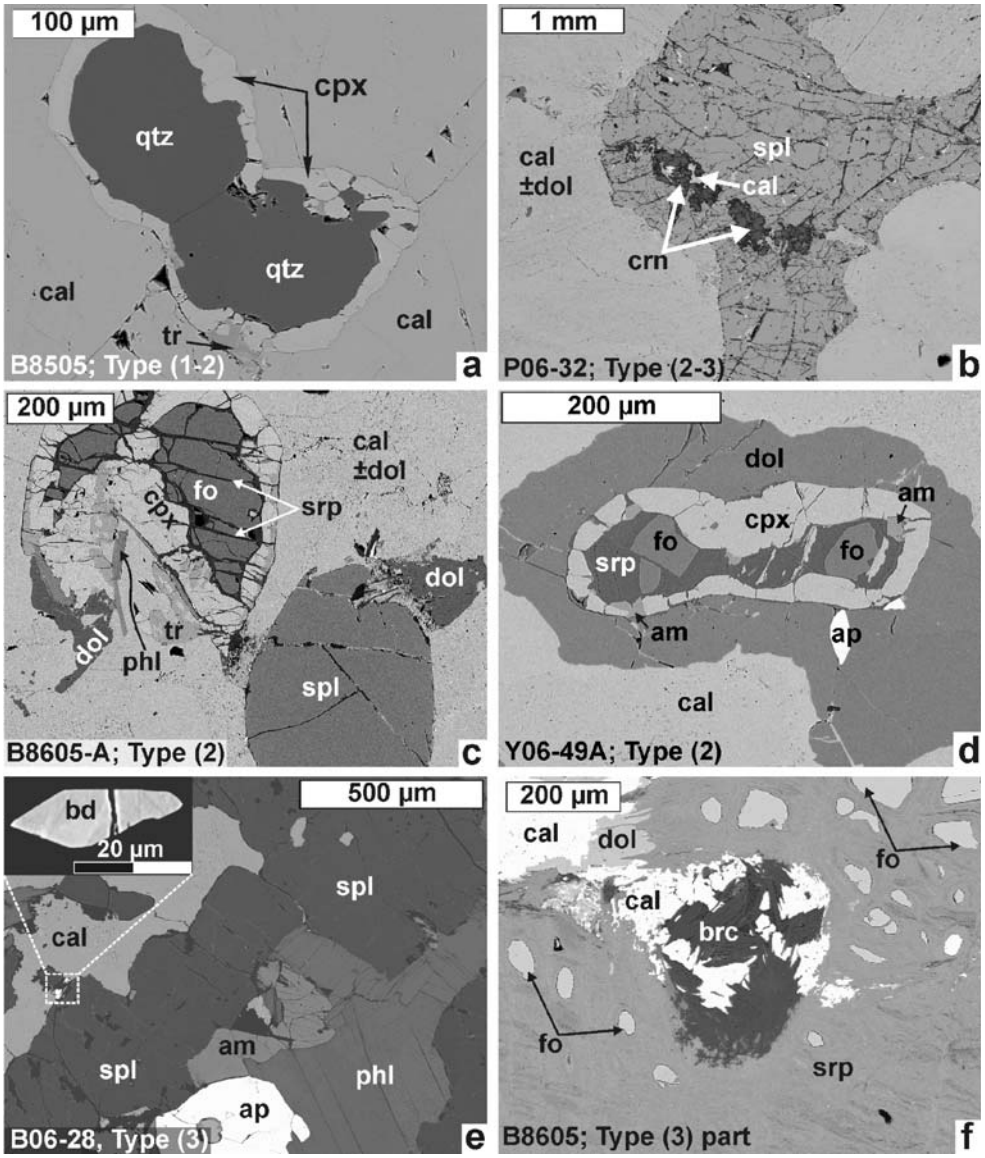

Fig. 4 Back-scattered electron images of representative Type (2) and Type (3) marbles; **a** clinopyroxene replacement textures around quartz in a calcite matrix with minor dolomite exolution lamellae; **b** inherited corundum inclusions in spinel. The carbonate matrix contains abundant dolomite exolution lamellae of various thickness; **c** forsterite + green spinel representing the peak-metamorphic assemblage. Forsterite becomes successively replaced by clinopyroxene; **d** clinopyroxene + dolomite corona texture replacing forsterite which subsequently becomes serpentinized; **e** occurrence of baddeleyite in a spinel-phlogopite bearing Type (3) marble; **f** retrograde brucite and serpentine replacing forsterite. Abbreviations: (am) amphibole, (ap) apatite, (bd) baddeleyite, (brc) brucite, (crn) corundum, (dol) dolomite, (fo) forsterite, (phl) phlogopite, (spl) spinel, (srp) serpentine, (tr) tremolite

Coarse-grained forsterite (200–500 µm) formed according to the prograde reaction (9) whereas 20–100 µm thick clinopyroxene coronas and dolomite rimming forsterite are considered to be products of the reverse reaction (9) (Fig. 4c,d):

$$1\ \text{diopside} + 3\ \text{dolomite} = 1\ \text{forsterite} + 4\ \text{calcite} + 2\ CO_2 \quad (9)$$

Type (3) dolomitic marbles

The Type (3) dolomite marbles appear as strongly weathered layers with intense serpentinization and chloritization. Primary matrix-dolomite is often cross-cut by an interconnected fracture network filled with late precipitated calcite. Single grains of baddeleyite (∅~30 µm) occur together with spinel and serpentine (Fig. 4e). According to experimental studies by Ferry et al. (2002), baddeleyite can form by the reaction:

$$\text{zircon} + 2\text{dolomite} = \text{baddeleyite} + \text{forsterite} + \text{calcite} + 2\ CO_2 \quad (10)$$

Retrograde reactions in the three marble types

In the Type (1) marbles, the retrograde breakdown of scapolite can be observed along fractures by the vapour-absent reaction (11):

$$1\ \text{scapolite} = 1\ \text{anorthite} + 1\ \text{calcite} \quad (11)$$

Grandite is locally replaced by epidote-quartz-calcite symplectites (Fig. 5a) in the Type (Ferry et al. 2002) marbles by the hydration reaction:

$$3\ \text{grossular} + 1\ CO_2 + 5\ H_2O = 2\ \text{epidote} + 3\ \text{quartz} + 5\ \text{calcite} \quad (12)$$

In the Type (2) and (3) marbles, pseudomorphic serpentine and brucite after forsterite are formed by reaction (13), (Fig. 4f):

$$2\ \text{forsterite} + 3\ H_2O = \text{serpentine} + \text{brucite} \quad (13)$$

Serpentinization of forsterite (Fig. 4c,d) along fractures and grain boundaries may be due to the hydration reaction:

$$3\ \text{forsterite} + 4\ H_2O\ (1) + SiO_2\ (aq) = \text{serpentine} \quad (14)$$

Fine-grained tremolite around diopside (Fig. 5b) indicates the reaction:

$$1\ \text{dolomite} + 4\ \text{diopside} + 1\ H_2O + 1\ CO_2 = 1\ \text{tremolite} + 4\ \text{calcite} \quad (15)$$

Tremolite is sometimes replaced by talc (Fig. 5b and c). This could be due to the H2O and CO2 consuming reaction (16):

$$1\ \text{tremolite} + 1\ \text{dolomite} + 1\ H_2O + 1\ CO_2 = 2\ \text{talc} + 3\ \text{calcite} \quad (16)$$

Pseudomorphic brucite along former dolomite exsolution lamellae (Fig. 5d) could indicate the reaction:

$$1\ \text{dolomite} + 1\ H_2O = 1\ \text{brucite} + 1\ \text{calcite} + 1\ CO_2 \quad (17)$$

Mineral chemistry

Wollastonite is usually pure end-member $CaSiO_3$ (Table 1)

Scapolite (Table 2) is a solid solution between meionite ($Ca_4Al_6Si_6O_{24}CO_3$) and mizzonite ($NaCa_3Al_5Si_7O_{24}CO_3$) with minor variations in Na_2O, Cl and SO_3. The meionite content ranges between 75 mol% and 80 mol%. Equivalent anorthite (EqAn) values were calculated using the normalization on the basis of Si+Al=12 (Shaw 1960; Evans et al. 1969) and C=1- Cl-S. EqAn contents of scapolite ranges between 58% and 75%. X_{CO3} was calculated using the equation $X_{CO3} = 1\text{-}X_{Cl}\text{–}X_{SO4}$, where X_{Cl}=Cl/[Cl+SO_4+CO_3] and X_{SO4}=SO_4/[Cl+SO_4+CO_3]. As X_{SO4} and X_{Cl} are low, this site is almost completely filled by CO_3^{2-}.

Grandite occurs as single grain-matrix garnet and as a reaction product after scapolite and scapolite-wollastonite. The garnets are grossular-rich (77–98 mol%) with up to 22 mol% andradite, hence the grandite solid solution is 96–99 mol% with minor almandine (Alm_{0-3}) and no spessartine or pyrope components (Table 3). In contact with clinopyroxene, grandite reaction rims show a well-developed compositional zoning. The grossular component reaches

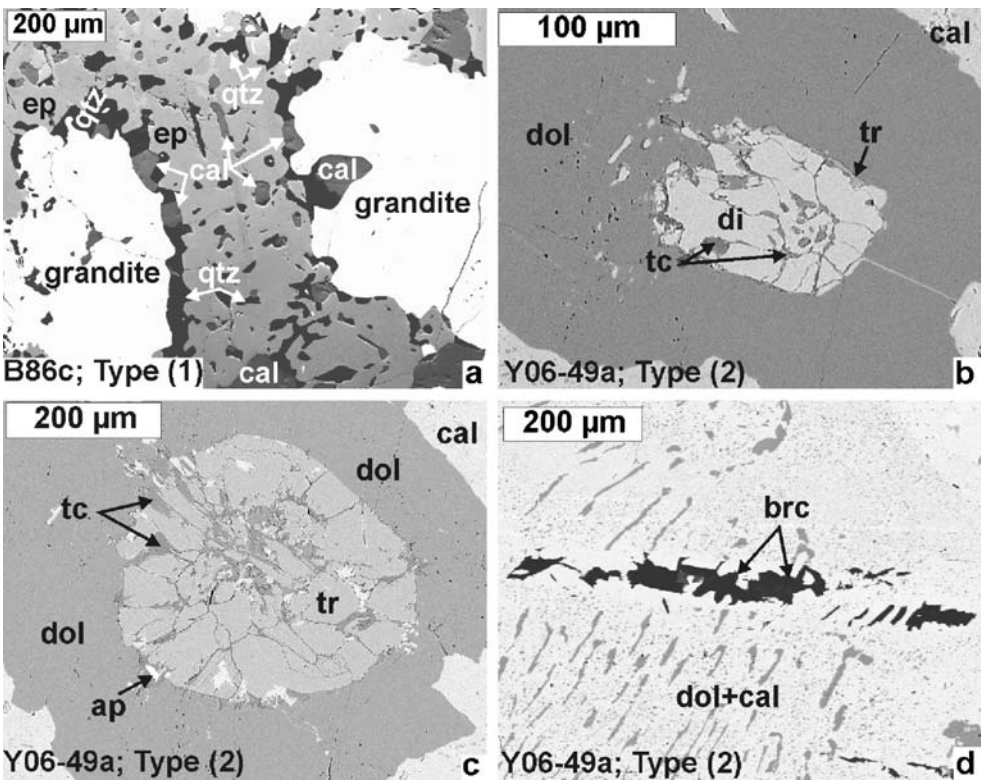

Fig. 5 Back scattered electron images of retrograde reaction textures in the Type (1) and (2) marbles. **a** epidote-quartz-calcite symplectites replacing grandite; **b** diopside with a dolomite corona replaced by tremolite and talc; **c** an aggregate of tremolite replacing a former diopside and surrounded by a dolomite corona that may have formed during diopside formation. Talc replaces tremolite; **d** pseudomorphic brucite is formed sub-parallel to former dolomite exsolution lamellae in the calcite matrix. Abbreviations: (ep) epidote

Table 1 Representative electron microprobe analyses of brucite, corundum, epidote, forsterite, spinel, talc, amphibole, titanite, wollastonite and baddeleyite. n.d. not determined

Sample	Brc B8605	crn Y0105	ep A06−1	ep A06−8	ol B86−B	ol Y06−49	Sp P06−31	sp Y0105	sp B8605	tc Y0105	am Y06−49a	am Y06−49a	ttn Y06−38	wol B06−21	wol A06−62		bdl B-28b1	bdl B-28b2
SiO_2	<0.2	<0.2	38.1	38.7	41.8	41.9	<0.2	<0.2	0.26	62.9	57.3	56.0	29.9	50.0	52.4	SiO_2	<0.2	<0.2
TiO_2	<0.1	<0.1	0.19	<0.1	<0.1	<0.1	<0.1	<0.1	<0.1	0.12	<0.1	0.12	37.7	b.d.l.	b.d.l.	TiO2	2.47	1.42
Al_2O_3	<0.2	100.1	26.0	27.3	<0.2	<0.2	66.2	64.6	68.6	<0.2	1.88	2.62	0.90	<0.2	<0.2	Al_2O_3	<0.2	0.28
Cr_2O_3	n.d.	n.d.	n.d.	n.d.	<0.1	<0.1	<0.1	0.28	<0.1	<0.1	n.d.	n.d.	<0.1	<0.1	<0.1	Cr_2O_3	<0.1	<0.1
Fe_2O_3	–	–	9.90	8.17	–	–	1.92	0.42	1.57	–	1.14	1.17	0.87	<0.1	–	Fe_2O_3	0.27	0.13
FeO	1.89	<0.1	–	–	2.17	0.39	11.4	10.1	1.47	3.90	1.6	1.52	–	<0.1	<0.1	FeO	<0.1	<0.1
MnO	<0.1	<0.1	0.16	0.32	<0.1	<0.1	<0.1	<0.1	<0.1	<0.1	<0.1	0.17	<0.1	<0.1	<0.1	MnO	<0.1	<0.1
ZnO	n.d	<0.2	n.d.	n.d.	<0.2	<0.2	<0.2	6.87	0.51	<0.2	n.d.	n.d.	<0.2	<0.2	<0.2	ZnO	<0.2	0.30
MgO	67.2	<0.2	<0.2	<0.2	55.3	57.2	20.3	16.7	26.8	30.0	23.4	22.8	<0.2	0.23	0.35	MgO	0.60	<0.2
CaO	0.29	<0.1	23.6	23.6	<0.1	<0.1	<0.1	<0.1	<0.1	<0.1	13.2	12.9	29.5	49.5	46.3	CaO	0.34	0.29
Na_2O	n.d.	n.d.	n.d.	n.d.	n.d.	n.d.	n.d.	n.d.	n.d.	n.d.	0.16	0.2	<0.03	<0.03	0.78	ZrO_2	92.4	95.2
H_2O	30.6	–	1.91	1.92	–	–	–	–	–	4.75	2.21	2.18	0.26	–	–	HfO_2	2.79	2.81
Total	99.9	100.1	99.9	100.0	99.2	99.6	99.8	98.9	99.2	101.6	100.9	99.6	99.0	99.7	99.8	Total	98.9	100.4
cation normalized																		
	1	2	8	8	3	3	3	3	3	7	15	15	3	4	4		1	1
Si	–	–	2.99	3.01	0.99	0.99	–	–	0.01	3.97	7.76	7.69	0.98	1.95	2.01	Si	–	–
Ti	–	–	0.01	–	–	–	–	–	–	0.01	0.01	0.01	0.93	–	–	Ti	0.04	0.02
Al	–	2.00	2.41	2.51	–	–	1.96	1.98	1.96	–	0.30	0.42	0.03	0.00	–	Al	0.00	0.01
Cr	–	–	–	–	–	–	–	0.01	–	–	–	–	–	–	–	Cr	–	–
Fe^{3+}	–	–	0.59	0.48	–	–	0.04	0.01	0.03	–	0.12	0.12	0.02	–	–	Fe^{3+}	0.00	0.00
Fe^{2+}	0.02	–	–	–	0.04	0.01	0.24	0.22	0.03	0.21	0.18	0.17	–	–	–	Fe^{2+}	–	–
Mn	0.00	–	0.01	0.02	–	–	–	–	–	–	–	0.02	–	–	–	Mn	–	–
Zn	–	–	–	–	–	–	–	0.13	0.01	–	–	–	–	–	–	Zn	–	0.00
Mg	0.98	–	–	–	1.96	2.01	0.76	0.65	0.97	2.82	4.72	4.66	0.01	0.01	0.02	Mg	0.02	0.00
Ca	0.00	–	1.99	1.97	–	–	–	–	–	0.01	1.91	1.90	1.03	2.07	1.91	Ca	0.01	0.01
Na	–	–	–	–	–	–	–	–	–	–	0.04	0.05	–	–	0.06	Zr	0.89	0.92
OH	2.00	–	1.00	1.00	–	–	–	–	–	2.00	2.00	2.00	0.06	–	–	Hf	0.02	0.02

Table 2 Representative electron microprobe analyses of scapolite. Calculated meionite activities are also given

Sample	B06-18				B06-28b			B8505-3			
	1 Rim	2 rim	3 rim	4 core	1 core	2 core	3 rim	1 rim	2 core	3 core	4 Rim
SiO_2	44.8	45.7	44.5	44.6	46.0	46.2	47.1	43.4	43.5	43.6	44.6
Al_2O_3	27.4	27.4	27.4	27.2	28.5	27.3	27.8	28.3	27.6	27.7	27.3
CaO	18.8	18.4	18.2	19.5	18.4	18.1	17.8	19.8	19.9	20.4	18.8
K_2O	0.32	0.26	0.23	0.19	< 0.1	0.20	0.11	0.17	0.17	< 0.1	0.25
Na_2O	3.00	3.15	2.98	2.66	2.73	2.81	3.04	3.12	2.72	2.70	3.25
SO_4	0.19	0.34	0.40	0.36	1.06	0.28	1.27	0.73	0.45	0.98	0.40
CO_2	4.34	4.22	4.36	4.38	4.11	4.46	4.04	4.21	4.28	4.08	4.17
Cl	0.23	0.31	0.12	0.11	0.21	0.16	0.20	0.11	0.13	0.10	0.27
	99.1	99.8	98.2	99.0	101.0	99.5	101.4	99.8	98.7	99.6	99.0
Cl corr.	0.05	0.07	0.03	0.02	0.05	0.04	0.05	0.02	0.03	0.02	0.06
Total	99.0	99.7	98.2	99.0	101.0	99.4	101.3	99.8	98.7	99.6	99.0
normalized on Si + Al = 12 and C = 1-Cl–S											
Si	6.97	7.03	6.95	6.98	6.94	7.07	7.07	6.79	6.87	6.87	6.97
Al	5.03	4.97	5.05	5.02	5.06	4.93	4.93	5.21	5.13	5.14	5.03
Ca	3.13	3.04	3.04	3.28	2.97	2.97	2.87	3.32	3.38	3.44	3.15
K	0.06	0.05	0.05	0.04	–	0.04	0.02	0.03	0.03	–	0.05
Na	0.90	0.94	0.90	0.81	0.80	0.83	0.89	0.95	0.83	0.82	0.99
S	0.02	0.03	0.04	0.04	0.10	0.03	0.12	0.07	0.04	0.10	0.04
C	0.92	0.89	0.93	0.94	0.85	0.93	0.83	0.90	0.92	0.88	0.89
Cl	0.06	0.08	0.03	0.03	0.05	0.04	0.05	0.03	0.03	0.03	0.07
X-meionit	0.76	0.75	0.76	0.80	0.79	0.77	0.76	0.77	0.80	0.81	0.75
eqAn	0.68	0.66	0.68	0.67	0.69	0.64	0.64	0.74	0.71	0.71	0.68
a-meionite	0.25	0.23	0.25	0.32	0.30	0.27	0.24	0.27	0.33	0.34	0.23
XCl	0.06	0.08	0.03	0.03	0.05	0.04	0.05	0.03	0.03	0.03	0.07
XSO_4	0.02	0.03	0.04	0.04	0.10	0.03	0.12	0.07	0.04	0.10	0.04
XCO_3	0.92	0.89	0.93	0.94	0.84	0.93	0.83	0.90	0.92	0.88	0.89

its maximum at the immediate contact with the relict grain of scapolite and decreases towards the rim and/or cpx-interface to an andradite-rich grandite composition (Fig. 3b,c).

In Type (1) marbles clinopyroxene is diopside with X_{Mg} = Mg/[Mg+Fe^{2+}+Fe^{3+}+Mn] between 0.75 and 0.99 (Table 4). Clinopyroxene in the Type (1c) assemblage of sample B06-18 shows a decrease in Fe content towards the rim. A similar decrease in the Fe content of clinopyroxene occurs in the Type (1b) assemblage. Clinopyroxenes from Type (2) marbles are generally diopside with small variations in X_{Mg}=0.91−0.98 (Table 4, B8605-A). Rare occurrences of single grains of diopside (Table 4, P06-32), often associated with green spinel, show a slight tendency to a lower X_{Mg} of about 0.91.

Olivine compositions are close to end-member forsterite (Table 1) with minor variations in FeO~0.39–2.17 wt.%.

Spinel is usually a solid-solution between $MgAl_2O_4$-$Fe^{2+}Al_2O_4$ with X_{Mg}=0.96-0.76, and minor Fe^{3+}. Some spinel contains up to 6.87 wt.% ZnO (Table 1).

Baddeleyite (Table 1) contains minor Ti (= 1.42–2.47 wt.%) and Hf (= 2.79–2.81wt. %), and corundum is pure Al_2O_3 (Table 1).

Amphibole (Table 1) is essentially a magnesiohornblende-tremolite solid-solution with an XMg~0.94 and Al^{IV} ranging from 0.24 to 0.31 (Mogessie et al. 2004).

Epidote occurs only as a retrograde reaction product after grandite with Fe^{3+} = 9.90 to 8.17 wt.%. (Table 1).

The Mg-content of matrix calcites representing partially pre-exsolved calcites with only minor amounts of dolomite exolution lamellae and of matrix calcites with coarse-grained dolomite exsolution lamellae is about 2.05 to 3.75 wt.%. Younger matrix calcites with larger amounts of fine-grained dolomite exsolution lamellae contain lesser amounts of Mg (= 0.45 to 1.78 wt.%).

Stable carbon and oxygen isotope data

Representative carbon and oxygen isotope values obtained from the carbonate fraction are listed in Table 5. The histograms in Fig. 6a–d show the relative distribution of stable $\delta^{18}O$ (Fig. 6a,c) and $\delta^{13}C$ (Fig. 6b,d) values in the three different marble types.

In Type (1) marbles, calcite is the only carbonate fraction. To estimate the stable isotope signature of marbles

Table 3 Representative electron microprobe analyses of grandite solid solutions. Calculated grossular activities are also given

Sample	A06-62					B06-18												
	1 rim	2 core	3 core	4 rim	5 core	1 core	2 rim	3 rim	4 core	5 core	6 core	7 rim	8 core	9 rim	10 core	11 rim	12 core	13 Rim
SiO_2	39.0	39.9	40.9	39.4	39.8	40.1	39.0	38.4	40.3	40.9	39.1	39.2	40.2	39.1	40.6	39.7	39.8	40.2
TiO_2	0.31	<0.1	<0.1	<0.1	<0.1	0.20	0.30	0.44	0.14	<0.1	0.21	0.36	<0.1	0.38	0.13	0.34	<0.1	<0.1
Al_2O_3	18.1	20.3	22.2	15.4	22.1	21.4	17.7	17.0	21.3	20.7	16.5	17.8	21.7	17.7	21.5	17.5	21.6	19.6
Fe_2O_3	6.46	3.28	–	7.65	–	0.16	5.14	6.03	0.24	0.34	6.05	3.76	–	4.03	0.31	4.70	0.15	1.97
FeO	–	0.11	0.55	1.70	0.62	1.14	1.26	0.75	1.49	1.42	1.62	1.67	0.80	1.58	1.53	2.32	0.84	1.71
MnO	0.12	<0.1	<0.1	<0.1	<0.1	0.11	0.15	0.27	<0.1	0.16	<0.1	<0.1	0.17	0.10	0.25	0.17	0.15	0.10
MgO	0.19	<0.2	<0.2	<0.2	<0.2	0.33	0.35	0.32	0.33	0.53	<0.2	<0.2	0.30	<0.2	0.24	0.23	0.43	<0.2
CaO	35.8	36.0	36.4	34.9	36.3	36.1	34.8	34.9	35.9	36.2	34.9	35.4	36.1	35.4	36.3	35.1	35.7	36.0
Na_2O	0.11	0.31	0.07	0.12	<0.03	<0.03	<0.03	<0.03	<0.03	<0.03	<0.03	<0.03	<0.03	<0.03	<0.03	<0.03	<0.03	<0.03
Total	100.1	99.8	100.1	99.2	98.8	99.6	98.7	98.1	99.8	100.1	98.4	98.2	99.2	98.4	100.9	100.0	98.7	99.5
normalization based on 8 cations																		
Si	2.99	3.02	3.06	3.08	3.02	3.03	3.03	3.01	3.04	3.07	3.06	3.05	3.04	3.05	3.04	3.05	3.03	3.06
Ti	0.02	–	–	–	–	0.01	0.02	0.03	0.01	–	0.01	0.02	–	0.02	0.01	0.02	–	–
Al	1.63	1.81	1.96	1.42	1.97	1.91	1.62	1.57	1.90	1.83	1.52	1.64	1.93	1.63	1.90	1.58	1.94	1.76
Fe^{3+}	0.37	0.19	–	0.45	–	0.01	0.30	0.36	0.01	0.02	0.36	0.22	–	0.24	0.02	0.27	0.01	0.11
Fe^{2+}	–	0.01	0.03	0.11	0.04	0.07	0.08	0.05	0.09	0.09	0.11	0.11	0.05	0.10	0.10	0.15	0.05	0.11
Mn	0.01	–	–	–	–	0.01	0.01	0.02	–	0.01	–	–	0.01	0.01	0.02	0.01	0.01	0.01
Mg	0.02	–	–	–	–	0.04	0.04	0.04	0.04	0.06	–	–	0.03	–	0.03	0.03	0.05	–
Ca	2.94	2.92	2.92	2.92	2.95	2.93	2.90	2.93	2.90	2.91	2.91	2.95	2.93	2.95	2.90	2.89	2.91	2.93
Na	0.02	0.05	0.01	0.02	–	–	–	–	–	–	–	–	–	–	–	–	–	–
Endmember in mol%																		
Grs	0.79	0.90	0.98	0.74	0.98	0.95	0.80	0.78	0.94	0.94	0.77	0.84	0.97	0.84	0.94	0.80	0.96	0.90
Andr	0.19	0.10	0.00	0.22	0.00	0.01	0.15	0.18	0.01	0.01	0.17	0.11	0.00	0.12	0.01	0.13	0.00	0.06
Alm	0.00	0.00	0.01	0.04	0.01	0.02	0.03	0.02	0.03	0.03	0.04	0.04	0.02	0.03	0.03	0.05	0.02	0.04
Prp	0.01	0.00	0.00	0.00	0.01	0.01	0.01	0.01	0.01	0.02	0.01	0.00	0.01	0.00	0.01	0.01	0.02	0.00
Sps	0.00	0.00	0.00	0.00	0.00	0.00	0.00	0.01	0.00	0.00	0.00	0.00	0.00	0.00	0.01	0.00	0.00	0.00
a-Grs	0.62	0.76	0.87	0.43	0.92	0.84	0.57	0.55	0.82	0.77	0.50	0.62	0.87	0.61	0.82	0.53	0.86	0.71

Table 4 Representative electron microprobe analyses of clinopyroxenes. (a) cpx reaction rim around forsterite; (b) single grains of cpx; (c) cpx-wo association; (d) cpx-grandite-scp-wo assemblage; (e) cpx-fo-spl assemblage

	B8605-A				B06-21		A06-62			B06-18			P06-32
Sample	1(a)	2(a)	3(b)	4(b)	3(c)	6(c)	3(c)	5(c)	2(d)	12(d)	7(d)	9(d)	1(e)
marbel type	1 & 2	1 & 2	1 & 2	1 & 2	1	1	1	1	1	1	1	1	2
SiO_2	55.0	54.8	52.8	54.3	53.3	53.5	55.2	54.5	53.8	52.8	52.5	54.0	51.0
TiO_2	0.21	0.11	0.65	0.14	<0.1	0.10	<0.1	<0.1	<0.1	0.65	<0.1	<0.1	0.52
Al_2O_3	0.97	0.74	2.62	0.98	0.05	<0.2	<0.2	0.53	0.62	2.62	0.97	0.40	5.41
Fe_2O_3	–	–	–	–	–	–	–	1.53	0.72	–	0.65	0.47	–
FeO	0.75	0.82	1.00	0.77	0.41	0.46	6.46	5.27	4.07	1.00	7.17	3.27	2.76
MnO	<0.1	<0.1	<0.1	<0.1	<0.1	<0.1	<0.1	<0.1	0.12	<0.1	0.11	0.15	<0.1
MgO	18.35	18.15	17.41	18.32	18.19	17.91	14.31	14.23	14.91	17.41	12.36	15.37	14.88
CaO	24.8	24.7	24.4	24.3	26.6	26.6	24.4	24.1	24.0	24.4	23.4	24.2	24.2
Na_2O	<0.03	<0.03	<0.03	<0.03	<0.03	<0.03	<0.03	0.63	0.31	<0.03	0.31	0.21	0.03
Total	100.0	99.4	98.9	98.8	98.6	98.6	100.4	100.8	98.5	98.9	97.4	98.2	98.8
Normalized based on 4 cations and 12 Oxygen													
Si	1.98	1.99	1.93	1.98	1.96	1.97	2.02	2.00	2.00	1.93	2.00	2.01	1.88
Ti	0.01	0.00	0.02	0.00	–	0.00	–	–	–	0.02	–	–	0.01
Al	0.04	0.03	0.11	0.04	0.00	–	–	0.02	0.03	0.11	0.04	0.02	0.24
Fe3	–	–	–	–	–	–	–	0.04	0.02	–	0.02	0.01	–
Fe2	0.02	0.02	0.03	0.02	0.01	0.01	0.20	0.16	0.13	0.03	0.23	0.10	0.09
Mn	–	–	–	–	–	–	–	–	0.00	–	0.00	0.00	–
Mg	0.99	0.98	0.95	1.00	1.00	0.98	0.78	0.78	0.83	0.95	0.70	0.85	0.82
Ca	0.96	0.96	0.96	0.95	1.05	1.05	0.96	0.95	0.96	0.96	0.96	0.97	0.96
Na	–	–	–	–	–	–	–	0.05	0.02	–	0.02	0.02	0.00
endmember proportions													
Diopside	0.92	0.93	0.87	0.91	0.99	0.99	0.76	0.78	0.83	0.87	0.72	0.74	0.77
Wollastonite	0.47	0.48	0.45	0.47	0.50	0.50	0.48	0.47	0.48	0.45	0.48	0.49	0.43
Enstatite	0.49	0.49	0.47	0.50	0.50	0.49	0.39	0.39	0.41	0.47	0.35	0.36	0.41
Ferrosilite	0.01	0.01	0.02	0.01	0.01	0.01	0.10	0.08	0.06	0.02	0.11	0.12	0.04
$CaAl_2SiO_6$	0.01	0.01	0.04	0.01	0.00	0.00	0.00	0.00	0.00	0.04	0.00	0.00	0.09
xMg Fe^{2+}	0.98	0.98	0.97	0.98	0.99	0.99	0.80	0.83	0.87	0.97	0.75	0.76	0.91
Al(IV)	0.02	0.01	0.07	0.02	–	–	–	–	–	0.07	–	–	0.12
Al(VI)	0.02	0.02	0.04	0.02	–	–	0.01	0.02	0.03	0.04	0.04	0.03	0.12

which experienced a very low extent of decarbonation reactions, pure silica-free Type (1) marble samples were chosen. The $\delta^{18}O$ values of these samples range between 18.36–21.19‰, $\delta^{13}C$ values are 1.11–2.33‰ (Table 5, no. 1–4). Siliceous Type (1) calcite marbles show $\delta^{18}O$ values between ~19–23‰, (Table 5, no. 5–56 and Figs. 6a and 7b) and only two samples show low $\delta^{18}O$ values of <19‰ (Table 5, no. 27 and 54). Calcite marbles containing wollastonite as a main constituent are depleted in ^{13}C, with $\delta^{13}C$ values of−3.02 to−1.97 (Figs. 6b and 7b; Table 5, no. 7, 20, 39).

Isotopic alteration occurs at the marble-gabbro contact. Within a distance of a few centimetres, $\delta^{18}O$ values are significantly reduced to 12.83–13.49‰ and $\delta^{13}C$ values are -0.88–0.33‰ (Figs. 6a,b and 7a,b; Table 5, no. 85–90). At the immediate marble-gneiss contact a less-pronounced depletion in heavy isotopes occurred, with $\delta^{18}O$ ranging between 15.11–17.56‰ and $\delta^{13}C$~−0.73–0.93‰ (Table 5, no. 91–100).

In Type (2) marbles (Table 5, no. 57–61), dolomite exsolution lamellae, reactant dolomite coronas (see reverse reaction 9 and Fig. 4c,d) and calcite are the carbonate fractions present. Type (2) marbles show a wide range in the $\delta^{18}O$ values from 13.83 to 20.13‰ (Figs. 6c and 7a). The $\delta^{13}C$ values of −0.30–1.93‰ lie within the values for Type (1) marble (Figs. 6d and 7a, Table 5, no. 57–61).

Type (3) marbles have generally lower $\delta^{18}O$=12.94–18.22‰ (Figs. 6c and 7a; Table 5, no. 62–84), $\delta^{13}C$ values range from −1.49–1.65‰ (Figs. 6d and 7a).

Discussion

Stable isotopes and their importance for the evaluation of fluid-rock dynamics during metamorphism

Stable isotope signatures may shed light on the origin and passageways of metamorphic fluids during metamorphism

Table 5 $\delta^{13}C$ and $\delta^{18}O$ values for the marbles of La Huerta Range. Values of $\delta^{13}C$ and $\delta^{18}O$ are given relative to V-PDB and V-SMOW respectively. The rock type and the associated mineral assemblages are also given

No.	Sample	δ13C	δ18O	Carbonate fraction	Latidute	Longitude	Rock description	Silicate mineral gy
1	A-06-59	1.114	18.360	cal	30°46′58.3″	67°31′6.7″	Type(1) white cal-marble	no silicate phases
2	A-06-69	2.117	21.197	cal	30°47′00.1″	67°31′3.4″	Type(1) white cal-marble	no silicate phases
3	Y-06-48	1.824	20.253	cal	31°24′13.9″	67°19′51.4″	Type(1) white marble	no silicate phases
4	B-06-9	2.330	19.209	cal	31°23″7.5″	67°20′11.4″	Type(1) white-yellow cal-marble	no silicate phases
5	A-06-56-I	0.021	20.177	cal	30°46′58.3″	67°31′6.7″	Type(1) granulite calc-silicate fold	scp-wol-grandite-cpx
6	A-06-56-II	-0.167	20.359	cal	–	–	Type(1) granulite calc-silicate fold	scp-wol-grandite-cpx
7	A-06-56-III	−1.971	19.893	cal	–	–	Type(1) granulite calc-silicate fold	scp-wol-grandite-cpx
8	A-06-56-IV	0.544	20.335	cal	–	–	Type(1) granulite calc-silicate fold	scp-wol-grandite-cpx
9	A06-62-I	0.980	22.518	cal	30°46′58.3″	67°31′6.7″	Type(1) white calcite marble	wol-qtz-grandite-cpx
10	A06-62-II	1.010	22.766	cal	–	–	Type(1) white calcite marble	wol-qtz-cpx
11	A06-62-III	0.770	22.683	cal	–	–	Type(1) white calcite marble	wol-qtz-cpx
12	A06-62-IV	0.990	22.993	cal	–	–	Type(1) white calcite marble	wol-qtz-cpx
13	A06-62-V	0.950	22.879	cal	–	–	Type(1) white calcite marble	wol-qtz-cpx
14	B06-18-I	0.510	20.570	cal	31°22′56.7‴	67°20′24.8‴	Type(1) marble	scp-grandite-cpx
15	B06-18-II	0.460	20.890	cal	–	–	Type(1) marble	scp-grandite-cpx
16	B06-18-III	0.640	20.982	cal	–	–	Type(1) marble	scp-grandite-cpx
17	B-06-21 1	0.430	19.766	cal	31°22′56.7″	67°20′24.8″	Type(1) white layer	–
18	B-06-21 2	0.480	19.591	cal	–	–	Type(1) white layer	–
19	B-06-21 3	0.320	19.189	cal	–	–	Type(1) brown layer	–
20	B-06-21 4	-3.020	21.663	cal	–	–	Type(1) white calc-silicate layer	wo-cpx
21	B-06-21 5	0.330	19.518	cal	–	–	Type(1) brown layer	–
22	B-06-21 6	0.430	19.271	cal	–	–	Type(1) white layer	–
23	B-06-21 A	0.820	19.786	cal	–	–	Type(1) white layer	–
24	B-06-21 B	0.740	19.529	cal	–	–	Type(1) white layer	–
25	B-06-21 C	0.590	19.415	cal	–	–	Type(1) white layer	–
26	B-06-21 D	0.820	19.622	cal	–	–	Type(1) brown layer	–
27	B-06-21 E	−0.140	18.240	cal	–	–	Type(1) white calc-silicate layer	wo-cpx
28	B-06-21 F	−0.010	19.230	cal	–	–	Type(1) white calc-silicate layer	wo-cpx
29	B-06-21 G	0.300	19.436	cal	–	–	Type(1) brown layer	-
30	B-06-21 H	−0.250	19.993	cal	–	–	Type(1) white calc-silicate layer	wo-cpx
31	B-06-21 I	0.850	19.415	cal	–	–	Type(1) white layer	–
32	B-06-21 II	0.170	19.147	cal	–	–	Type(1) white calc-silicate layer	wo-cpx
33	B-06-21 III	0.600	19.178	cal	–	–	Type(1) white layer	–
34	B-06-21 IV	0.310	19.426	cal	–	–	Type(1) white calc-silicate layer	wo-cpx
35	B-06-21 J	0.590	19.611	cal	–	–	Type(1) white layer	–
36	B-06-21 K	0.570	19.570	cal	–	–	Type(1) brown layer	–
37	B-06-21 V	0.880	20.106	cal	–	–	Type(1) white layer	–
38	B-06-21 VI	0.570	19.127	cal	–	–	Type(1) brown layer	–
39	B-06-21 VII	−2.360	20.446	cal	–	–	Type(1) white calc-silicate layer	wo-cpx
40	B-8505 I	1.520	19.673	cal	31°22′57″	67°20′24″	Type(1) white cal-marble	qtz-cpx
41	B-8505 II	1.870	19.003	cal	–	–	Type(1) white cal-marble	qtz-cpx
42	B-8505 III	1.600	19.879	cal	–	–	Type(1) white cal-marble	qtz-cpx
43	B-8505 IV	1.700	19.951	cal	–	–	Type(1) white cal-marble	qtz-cpx
44	B-8505 IX	0.680	20.147	cal	–	–	Type(1) white cal-marble	qtz-cpx
45	B-8505 V	1.750	20.065	cal	–	–	Type(1) white cal-marble	qtz-cpx
46	B-8505 VI	1.740	20.065	cal	–	–	Type(1) white cal-marble	qtz-cpx
47	B-8505 VII	1.720	19.982	cal	–	–	Type(1) white cal-marble	qtz-cpx
48	B-8505 VIII	1.200	19.601	cal	–	–	Type(1) white cal-marble	qtz-cpx
49	B-8505 X	0.500	19.941	cal	–	–	Type(1) white cal-marble	qtz-cpx
50	B-8505 XI	0.400	20.158	cal	–	–	Type(1) white cal-marble	qtz-cpx
51	B-8505 XII	0.270	20.178	cal	–	–	Type(1) white cal-marble	qtz-cpx
52	B-8505 XIII	−0.020	19.797	cal	–	–	Type(1) white cal-marble	qtz-cpx
53	B-8505 XIV	0.040	19.890	cal	–	–	Type(1) white cal-marble	qtz-cpx
54	B-8605-A II	0.270	18.457	cal-dol	31°22′57″	67°20′24″	Type(1) white marble	–

Table 5 (continued)

No.	Sample	δ13C	δ18O	Carbonate fraction	Latidute	Longitude	Rock description	Silicate mineral gy
55	B-8605-I	0.213	19.506	cal	31°22′57″	67°20′24″	Type(1) cal-marble	–
56	B-8605-II	0.370	19.100	cal	–	–	Type(1) cal-marble	cpx
57	B-8605-A I	0.270	15.601	cal-dol	31°22′57″	67°20′24″	Type(2) cal-dol marble	cpx-fo-sp
58	B-8605-A V	−0.300	17.570	cal-dol	–	–	Type(2) cal-dol marble	cpx-fo-sp
59	B-8605-III	−0.076	17.596	cal	31°22′57″	67°20′24″	Type(2) cal-dol marble	cpx
60	B-8605-IV	0.213	20.138	cal	–	–	Type(2) cal-dol marble	phl
61	Y-0105	1.932	13.833	cal-dol	31°24′13.9″	67°19′51.4″	Type(2) cal-dol marble	tr-cpx-fo-sp-srp
62	AN-06-78-I	−0.359	13.945	cal-dol	31°20′40.2″	67°18′38.7″	Type(3) serpentinized dol-marble	srp
63	AN-06-78-II	−0.293	14.191	cal-dol	–	–	Type(3) serpentinized dol-marble	srp
64	B-8605-A III	−0.770	16.364	cal-dol	31°22′57″	67°20′24″	Type(3) serpentinized marble	srp-fo-sp
65	B-8605-A IV	0.040	17.890	cal-dol	–	–	Type(3) serpentinized marble	srp-fo-sp
66	B-8605-V	−1.487	14.701	cal-dol	31°22′57″	67°20′24″	Type(3) marble	srp-fo-phl
67	P37-I	1.178	15.533	cal-dol	31°24′45.3″	67°20′16.9″	Type(3) marble	–
68	P37-III	−0.347	15.012	cal-dol	–	–	Type(3) marble	srp-chl
69	P37-IV	−0.318	14.796	cal-dol	–	–	Type(3) marble	srp-chl
70	R84-I	−0.181	12.939	cal-dol	31°25′13.2″	67°22′44.6″	Type(3) marble	srp-chl
71	R84-II	0.529	17.346	cal-dol	–	–	Type(3) marble	srp-chl
72	R84-III	−0.792	13.844	cal-dol	–	–	Type(3) marble	srp-chl
73	R84-IV	−0.482	13.593	cal-dol	–	–	Type(3) marble	srp-chl
74	Y-0105A-I	1.653	14.547	cal-dol	31°24′13.9″	67°19′51.4″	Type(3) marble	srp-sp-chl
75	Y-0105A-II	0.596	14.891	cal-dol	–	–	Type(3) serpentinized marble	srp-sp-chl
76	Y-0105A-III	0.319	15.025	cal-dol	–	–	Type(3) serpentinized marble	srp-sp-chl
77	Y-0105A-IV	0.484	14.917	cal-dol	–	–	Type(3) serpentinized marble	srp-sp-chl
78	Y-0105A-V	0.371	14.904	cal-dol	–	–	Type(3) serpentinized marble	srp-sp-chl
79	Y-0105A-VI	−0.012	15.088	cal-dol	–	–	Type(3) serpentinized marble	srp-sp-chl
80	Y-0105A-VII	−0.451	15.167	cal-dol	–	–	Type(3) serpentinized marble	srp-sp-chl
81	Y-06-49-I	0.772	16.857	cal-dol	–	–	Type(3) marble	–
82	Y-06-49-II	1.397	16.255	cal-dol	–	–	Type(3) marble	–
83	Y-06-49-III	0.777	18.222	cal-dol	–	–	Type(3) marble	–
84	Y-06-49-IV	0.517	16.606	cal-dol	–	–	Type(3) marble	srp-brc
85	AN-06-80-I	0.332	13.490	cal	31°20′40.2″	67°18′38.7″	Type(1) marble-gabbro contact	cpx
86	AN-06-80-II	0.316	13.132	cal	–	–	Type(1) marble-gabbro contact	cpx
87	AN-06-80-III	0.202	13.186	cal	–	–	Type(1) marble-gabbro contact	cpx
88	AN-06-80-IV	−0.200	13.074	cal	–	–	Type(1) marble-gabbro contact	cpx
89	AN-06-80-V	−0.148	13.021	cal	–	–	Type(1) marble-gabbro contact	cpx
90	AN-06-80-VI	−0.886	12.830	cal	–	–	carbonate inclusion in gabbro	cpx-scp-ep
91	B-06-16-I	0.930	16.908	cal	31°22′56.7″	67°20′24.8″	Type(1) marble-gneiss contact	–
92	B-06-16-II	0.855	17.027	cal	–	–	Type(1) marble-gneiss contact	–
93	B-06-16-III	0.805	16.862	cal	–	–	Type(1) marble-gneiss contact	–
94	B-06-16-IV	0.497	16.787	cal	–	–	Type(1) marble-gneiss contact	–
95	B-06-16-V	0.473	16.380	cal	–	–	Type(1) marble-gneiss contact	–
96	B-06-16-VI	0.208	16.598	cal	–	–	Type(1) marble-gneiss contact	–
97	B-06-16-VII	−0.115	15.113	cal	–	–	Type(1) marble-gneiss contact	–
98	B-06-16-VIII	−0.737	15.614	cal	–	–	Type(1) marble-gneiss contact	–
99	B-8605-A VI	0.480	17.488	cal-dol	–	–	Type(1) marble-gneiss contact	cpx-qtz
100	B-8605-A VII	0.310	17.560	cal-dol	–	–	Type(1) marble-gneiss contact	cpx-qtz
101	A-06-74	0.992	13.053	cal	30°46′57.6″	67°30′53.1″	Type(1) marble-pegmatite contact	–

(Shieh and Taylor 1969; Baumgartner and Ferry 1991; Nabelek 1991; Abart 1995; Povoden et al. 2002). In this study, carbon and oxygen isotopes have been used to evaluate the fluid/rock evolution and the potential influence of any externally derived fluids (e.g. SiO_2(aq) metasomatism) not in isotopic equilibrium with the host. To investigate small-scale isotopic variations, material was collected from across banded samples using a dentist drill. For bulk-rock carbonate isotope geochemistry, multiple analyses were made on hand specimens, whereas centi-

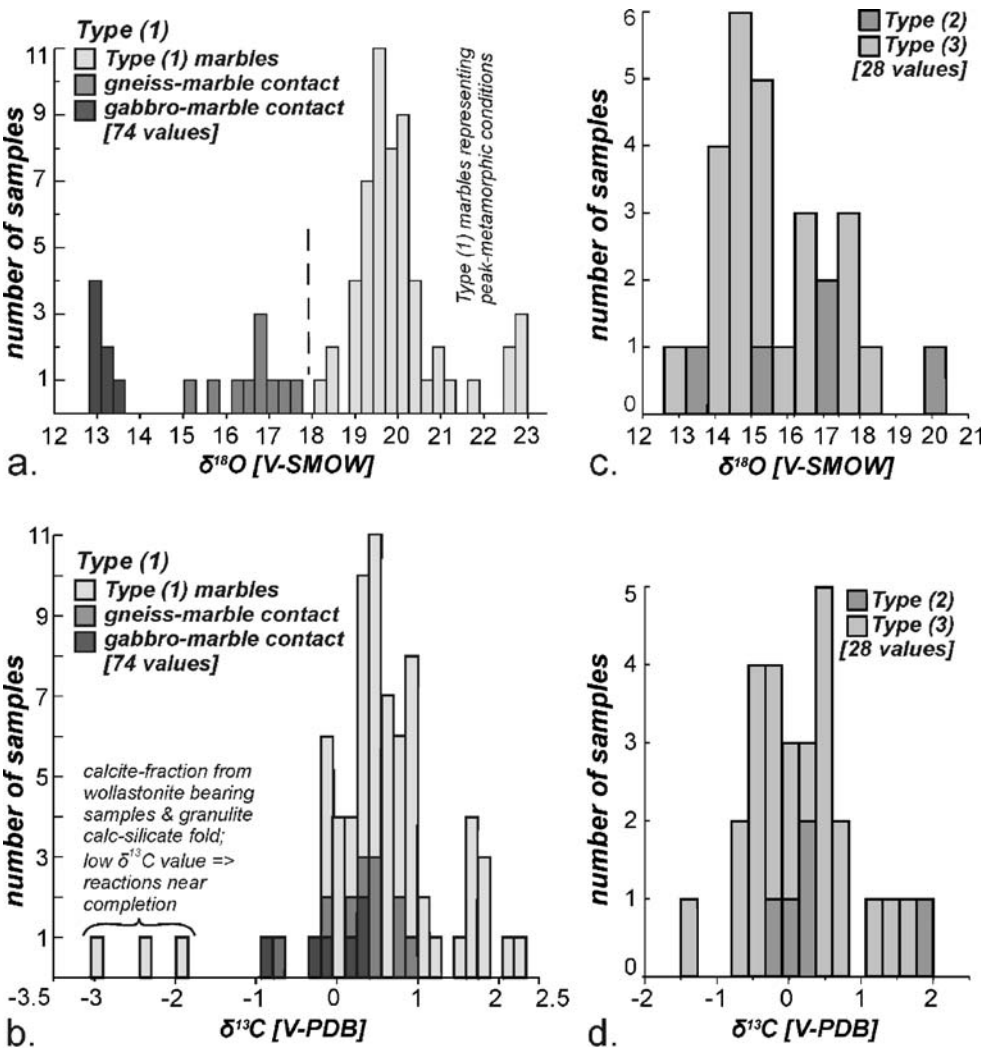

Fig. 6 Histograms of $\delta^{13}C$ and $\delta^{18}O$ isotope values from Type (1), (2) and (3) marbles; **a** the majority of the $\delta^{18}O$ values for Type (1) marbles is between 18.24 and 21.63‰. Centimetre-wide metasomatic reaction rims at a marble-gneiss and marble-gabbro contact lead to a depletion in $\delta^{18}O$ values to 15.11-17.56‰ and 12.83-13.49‰ [SMOW] respectively; **b** the majority of $\delta^{13}C$ values of the Type (1) marbles is between -0.2 to 0.88‰ [PDB] whereas wollastonite-bearing samples and samples taken from a fold in granulite-facies calc-silicate are depleted in $\delta^{13}C$; (c) $\delta^{18}O$ values of the Type (2) and (3) marbles are generally below 18‰ with lowest values of around 13‰; (d) the $\delta^{13}C$ values of the Type (2) and (3) are similar to the values of Type (1) marbles, except one $\delta^{13}C$ values at -1.48‰ taken from a serpentinized forsterite pocket

metre wide metasomatic contact zones between marble-gabbro and marble-gneiss were treated as separate samples. Veins and fissures that potentially provided a relatively late fluid-path-network are not considered here. It was not possible to make bulk-rock chemical analyses of each layered calc-silicate sample, since the thickness of each layer is in the range of 2 to 5 mm. Hence the stable isotope geochemistry of the carbonate fraction remaining after decarbonation reactions could not be correlated in detail.

The effect of metamorphic fluids liberated by devolatilization reactions on the stable isotope composition of the carbonate and other mineral fractions has been used in many terrains to study fluid-rock interaction (e.g. Gregory and Criss 1986; Valley 1986; Ferry and Dipple 1992; Bhowmik et al. 1995; Cartwright and Buick 1995; Gallien et al. 2007). In geological environments two end-member processes are used to describe fluid release by devolatilization reactions: (1) batch-devolatilization ("closed system"), where the volatile reaction products remain at the reaction site for some time before being released, (Nabelek et al. 1984) and; (2) Rayleigh devolatilization ("open system"), a continuous escape of aliquot amounts of volatiles from the reaction site (Rumble 1982; Valley 1986). Natural devolatilization reactions fall between these two end-member cases. The tendency of the volatile component CO_2 to incorporate more of the heavier isotopes ^{18}O and ^{13}C than the newly formed mineral assemblage causes a successive depletion in ^{18}O and ^{13}C of the remaining mineral and carbonate fractions, respectively (Nabelek et al. 1984; Brown et al. 1985). Experimental studies on equilibrium textures in carbonates show fast textural equilibration (within hours) at metamorphic conditions (Olgaard and Evans 1988; Holness and Graham 1991). Hence an interconnected pore and fracture network from the time before metamorphism and/or any earlier stage of metamorphism would be erased by matrix calcite reequilibration during heating. In a general sense fluid flow within a rock volume can occur by pervasive percolation along grain boundaries and by channelized fluid flow along fractures (eg. hydro-fracturing), faults, shear zones and lithological boundaries.

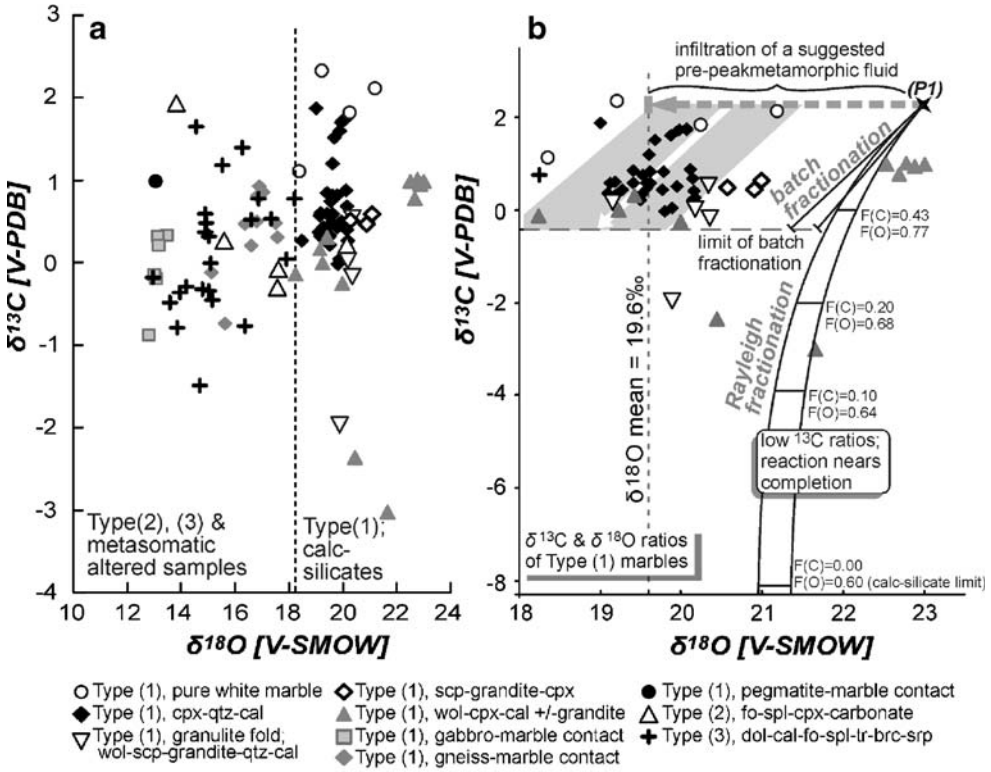

Fig. 7 **a** Stable isotope characteristics of Type (1), (2) and (3) marbles. The stippled vertical line indicates the $\delta^{18}O$ limit of Type (1) marbles. The Type (2) and (3) marbles are more depleted in $\delta^{18}O$ than Type (1) marbles **b** (P1) Indicates the initial carbon-oxygen ratio of a suggested pre-metamorphic precursor rock where $\delta^{13}C$ = 2.3‰ and $\delta^{18}O$ =~22 to 23‰ (Veizer et al. 1989). The stippled grey arrow indicates infiltration of a pre-peak-metamorphic fluid depleted in $\delta^{18}O$. Straight lines indicate a calculated coupled O-C trend for Batch fractionation (closed-system). White arrow indicates the depletion in $\delta^{18}O$ of the measured samples during prograde batch devolatilization. The limit of batch fractionation is indicated by the horizontal grey stippled line. Fluid liberation according to Rayleigh fractionation (solid curves) constrains a stronger depletion in $\delta^{13}C$ for some wo-scp-cpx-grandite-cal-qtz bearing samples. Fractionation factors for metamorphic temperatures are $\alpha^{13}C(CO_2\text{-rock})$ = 1.0027 (Rosenbaum, 1994) and $\alpha^{18}O(CO_2\text{-rock})$ = 1.0041 (Zheng 1994) and 1.033 (smaller shift of $\delta^{18}O$ corresponds to α = 1.033, Rosenbaum, 1994). Large depletion in ^{13}C only occurs as reactions near completion and as nearly all carbon is converted to CO_2. F = remaining mole-fraction of carbon and oxygen in the rock. The geometry of the Rayleigh and batch fractionation paths is calculated following Valley (1986)

Because of the plastic behaviour of calcite in high- and low-T regimes (De Bresser and Spiers 1997), hydro-fracturing is unlikely for the Type (1) marbles. This high tensile strength, at least for the Type (1) calcite marbles, would minimize the extent of grain boundary fluid flow towards a major fluid channel-way, for example lithological boundaries, folds and faults. Thus, processes close to batch-devolatilization are the most likely processes for coupled $\delta^{13}C$-$\delta^{18}O$ depletion in the Type (1) marbles.

Stable isotope alteration at marble-gabbro and marble-gneiss contact

Centimetre-scale isotope alteration occurs at the immediate marble–gneiss contact and leads to $\delta^{18}O$ values of 15.11–17.56‰ (Figs. 6a and 7a, Table 5, no. 91–100). This is consistent with the studies of Thompson and Connolly (1992), who ascribed significant focused fluid flow along lithological contacts, faults and shear zones. $\delta^{18}O$ values from 14–16 ‰ for low-grade metapelites have been reported by Cartwright et al. (1995). Thus the gneiss units are likely to be the fluid source for such centimetre-scale metasomatic zones in the Type (1) marbles.

Mixing of fluids generated by decarbonation in the host and magmatic fluids having $\delta^{18}O$~7–12‰ (Taylor and Sheppard 1986) would lead to relatively light oxygen isotope compositions. Measured $\delta^{18}O$ values at the immediate marble-gabbro contact of 12.83–13.49‰ (Figs. 6a and 7a, Table 5, no. 85–90) are the average between an inferred intermediate magmatic value of $\delta^{18}O$~9.2‰ and δ18O values of ~ 19.6‰ that are not affected by isotope alteration. Diffusion controlled major element metasomatism (eg. SiO_2(aq), Al_2O_3(aq)) could not be observed in either case.

Stable isotope characteristics of the Type (1) marbles

$\delta^{18}O$ values between 19–20.4 ‰ (Figs. 6a and 7b, Table 5, no. 1-65) for the calcite fraction are slightly below primary

sedimentary values (in the range of $\delta^{18}O$~22–23‰; Veizer et al. 1989). Based on $\delta^{13}C$ values, the peak-metamorphic Type (1) marbles are divided in two groups (Fig. 7b); (a) $\delta^{13}C$ values above the limit of Batch fractionation between −0.25 and 1.87‰ and; (b) $\delta^{13}C$ values below the limit of Batch fractionation between −3.02‰ and −1.97‰.

(a) $\delta^{13}C$ and $\delta^{18}O$ values above the limit of batch fractionation: The depletion of the rock in the heavy isotopes varies with the amount of devolatilization and can be written according to the equation for batch devolatilization (Valley 1986):

$$\delta_f = \delta_i - (1 - F)\,1000 ln a \quad (18)$$

where δf and δi are the final and initial isotope values of the rock in parts per mill (‰), F is the mole fraction of the element in question that remains in the rock and α is the fractionation factor.

Applying equation (18) to measured values from La Huerta Range samples, the δ_f(oxygen) = 19.76‰, when the initial δ_i(oxygen) = 21.19‰ (measured value of pure calcite marbles, Table 5, no. 2), F(oxygen) = 0.65 and α = 1.0041 (fractionation factor of oxygen for calcite-CO_2 given by Zheng (1994). If the value of F(oxygen) = 0.6 it corresponds to the "calc-silicate limit" (Valley 1986). Based on the remaining oxygen available in the rocks at the time decarbonation reactions stopped, F can be calculated, for example for the wollastonite-forming reaction (1). When reaction (1) nears completion the total amount of oxygen in the rock is incorporated in wollastonite. F(oxygen) = 0.6 can be calculated as: (3oxygen[products without CO_2])/(5oxygen [educt phases]). Hence a larger decrease in $\delta^{13}C$ occurs when the reaction nears completion and all carbon is converted to CO_2. In this extreme case F(oxygen) = 0.6 and F(carbon) = 0.0.

A final carbon value of δ_f(carbon) = −0.26‰ is calculated when initial δ_i(carbon) = 2.12‰ (measured value of pure calcite marbles, Table 5, no. 2), F(carbon) = 0.12 and α = 1.0027 (fractionation factor of carbon for calcite-CO_2 given by Rosebaum (1994). F(oxygen) and F (carbon) were chosen to be 0.65 and 0.12, respectively, for the best fit between calculated and measured values. Thus decarbonation reactions did not progress to completion and not all carbonate was converted to CO_2. Insufficient availability of siliceous impurities to drive decarbonation reactions could be the reason for an intermediate F(oxygen) value of 0.65. The degree of coupled ^{13}C-^{18}O depletion in Fig. 7b is generally positively correlated with the amount of decarbonation. Wollastonite-scapolite-grandite-bearing samples show a larger depletion in ^{13}C and ^{18}O than samples where only minor decarbonation reactions contribute to a coupled C-O depletion, e.g. in some clinopyroxene-quartz marbles and silica-free marbles.

(b) Samples from this group are Type (1b) and (1d) marbles from folded granulite-facies calc-silicate, which have more strongly depleted $\delta^{13}C$ values between −3.02‰ and −1.97‰. If externally derived fluids are negligible, such depletion in the heavy carbon isotope can only be reached by Rayleigh fractionation. In their derivation of the Rayleigh fractionation Broecker and Oversby (1971, p. 166) give the following formulation:

$$\delta_f - \delta_i = 1000\left(F^{(a-1)} - 1\right) \quad (19)$$

Applying equation (19) with the assumption that decarbonation reactions near completion, values of final δ_f(carbon) = −2.362‰, and final δ_f(oxygen) = 19.58‰; when F(oxygen) = 0.67, F(carbon) = 0.19, δ_i(oxygen) = 21.19‰, δ_i(carbon) = 2.12‰ and α = 1.0041 (Zheng 1994).

The results of the calculated and observed coupled C-O depletion imply that the majority of the calcite-marbles of La Huerta Range behaved as a closed system, where no fluid exchange between the surrounding rocks and the marbles took place at peak metamorphic conditions. The weak coupled depletion of $\delta^{18}O$-$\delta^{13}C$ (Fig. 7b) was caused by a combination of Batch- and Rayleigh-fractionation. Most of the samples experienced devolatilization close to batch devolatilization, where the evolved fluid was in local equilibrium with the rock for some time. This group includes all Type (1a) and the majority of Type (Zheng 1994) marbles.

The processes of fluid liberation during prograde metamorphism of wollastonite-clinopyroxene (Fig. 2b and c) and wollastonite-scapolite-clinopyroxene-grandite-quartz assemblages in folded granulite-facies calc-silicate (Fig. 2f) were close to Rayleigh devolatilization. A more pronounced depletion of ^{13}C (Table 5, no. 7, 20, 39) is reached by a more effective open system, due to a continuous removal of the liberated CO_2 fluid from the reaction site. Another possibility to explain the $\delta^{13}C$ depletion is metasomatic influx of CO_2 rich fluids depleted in ^{13}C e.g. fluids that originated in the deep crust and/or related plutonic rocks (e. g. Valley and O'Neil 1981; Moecher et al. 1994; Vry et al. 1988).

Stable isotope characteristics of the Type (2) and (3) marbles

The effect of late, channelized, externally derived H_2O-rich fluid infiltration along a capillary and vein system caused intense hydration of forsterite-rich dolomites and led to the precipitation of low-T calcite depleted in ^{18}O values ranging from 13.3 to 18.2‰ (Figs. 6c and 7a, Table 5, no. 57–84). A larger extent of dolomite-consuming decarbonation reactions in the Type (2) and (3) marbles possibly supports a higher volume loss during decarbonation. Thus originally dolomite-rich lithologies could be more susceptible to infiltration of external fluid depleted in ^{18}O. The lack of peak-metamorphic

unaltered Type (3) marbles excludes them for interpreting the fluid evolution during metamorphism.

Phase relations in (pseudo)-petrogenetic grids

T-a_{CO2} grids (Figs. 8a, 9), a P-a_{CO2} grid (Fig. 8b), T-X_{CO2} grids (Fig. 10a,b) and μH_2O-μCO_2 diagrams (Fig. 11a and b)

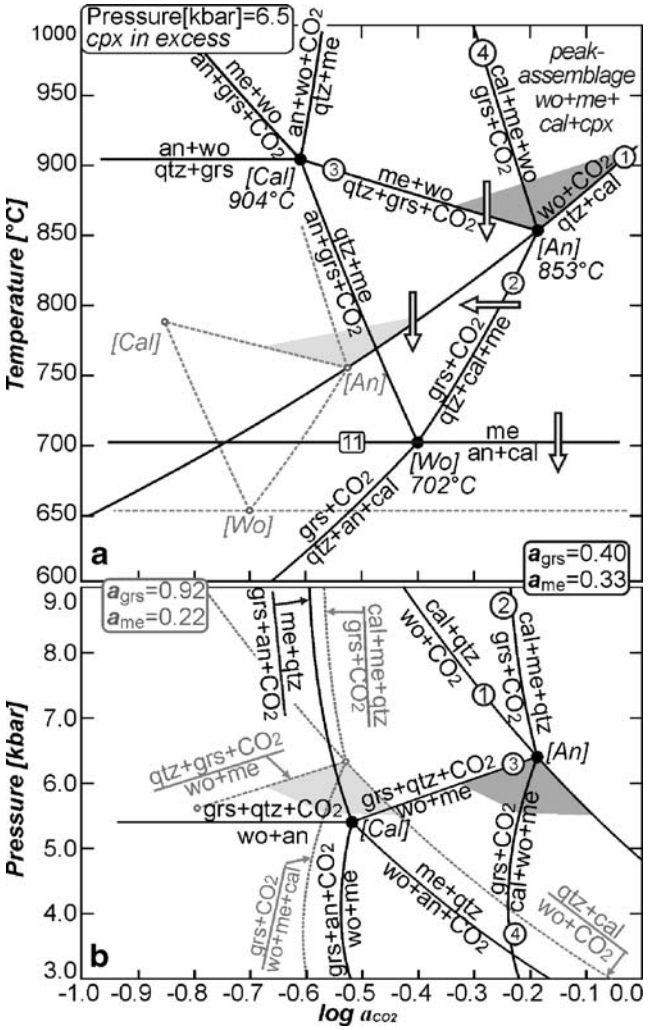

Fig. 8 Black solid curves represent a_{grs}= 0.40 and a_{me} = 0.33. Grey stippled curves represent a_{grs} = 0.92 and a_{me} = 0.22. **a** Isobaric T-a_{CO2} grid for the Type (1) marbles in the CASC system at 6.5 kbar using activity corrections for grossular and meionite to account for natural compositions and textural relations. The arrow heads indicate grandite- and wollastonite-forming reactions and the breakdown of scapolite. The shaded areas indicate the T-a_{CO2} conditions for the two different grandite-meionite (me) compositions and the displacement of the pseudo-invariant points [An], [Cal] and [Wo]. **b** A partial isothermal P-a_{CO2} grid for the Type (1) marbles in the CASC system at 850°C (black solid curves) and 750°C (grey stippled curves) using reduced activities for grossular and meionite. The two shaded areas represent the position of the mineral assemblages at the two different compositions. Numbered reaction are those used in the text. The displacement of the pseudo-invariant point [An] indicates isobaric cooling and lowering in the activity of CO_2

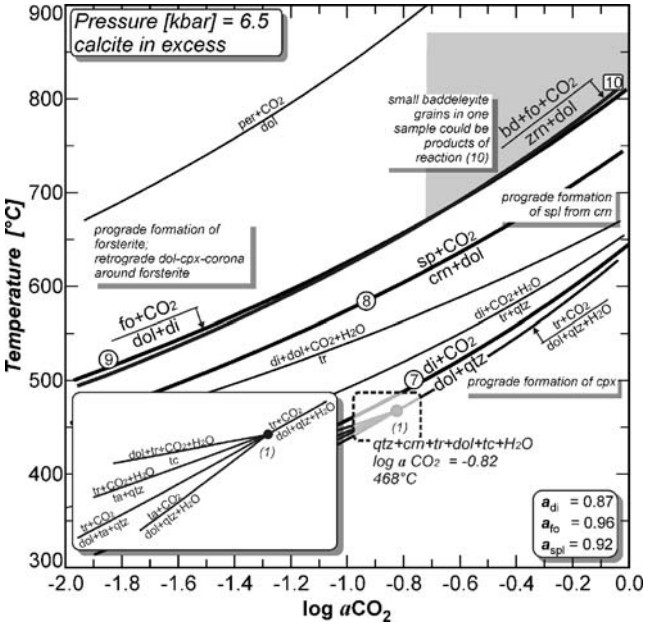

Fig. 9 An isobaric T-a_{CO2} diagram showing phase equilibria in the CMASCH model system for the Type (2) and (3) marbles. Activity corrections were performed for diopside, forsterite and spinel. Numbered reactions are those used in the text. The shaded area represents the possible position of the peak-metamorphic mineral assemblage

were calculated with the program PERPLEX (Connolly 1990 updated July 2007) using the July 2002 updated thermodynamic dataset (file hp02ver.dat) from Holland and Powell (1998). Due to different MgO contents, the two simplified chemical systems CASC (CaO, Al_2O_3, SiO_2, CO_2) and CMASCH (CaO, MgO, Al_2O_3, SiO_2, CO_2, H_2O) were used for Type (1) and Type (2), (3) marbles respectively. Reduced mineral activities were used to account for non-CASC and CMASCH components in real mineral compositions. The activity–composition relations of grossular (a_{Grs} = 0.40–0.92), forsterite (a_{Fo} = 0.96), spinel (a_{Spl} = 0.92), diopside (a_{di} = 0.87) and clinozoisite (a_{cz} = 0.82) were calculated using the program AX (updated version May 2007) of Holland and Powell (1998). Applying the experimentally-based disordered scapolite model of Baker and Newton (1995), the meionite activity at 850°C was found to range from a_{Me} = 0.22 in rims to a_{Me} = 0.33 in cores. Based on these activity data, activity-corrected petrogenetic grids were calculated which show stability fields separated by pseudo-univariant lines and pseudo-invariant points. Such diagrams are only valid for the investigated mineral compositions at specific P-, T-fluid conditions at which the peak metamorphic mineral assemblage was formed. The peak metamorphic pressure of 6.5 kbar was obtained by GASP barometry from nearby garnet-sillimanite gneisses by Schneider et al. (2006), Otamendi et al. (2007) and Delpino et al. (2008).

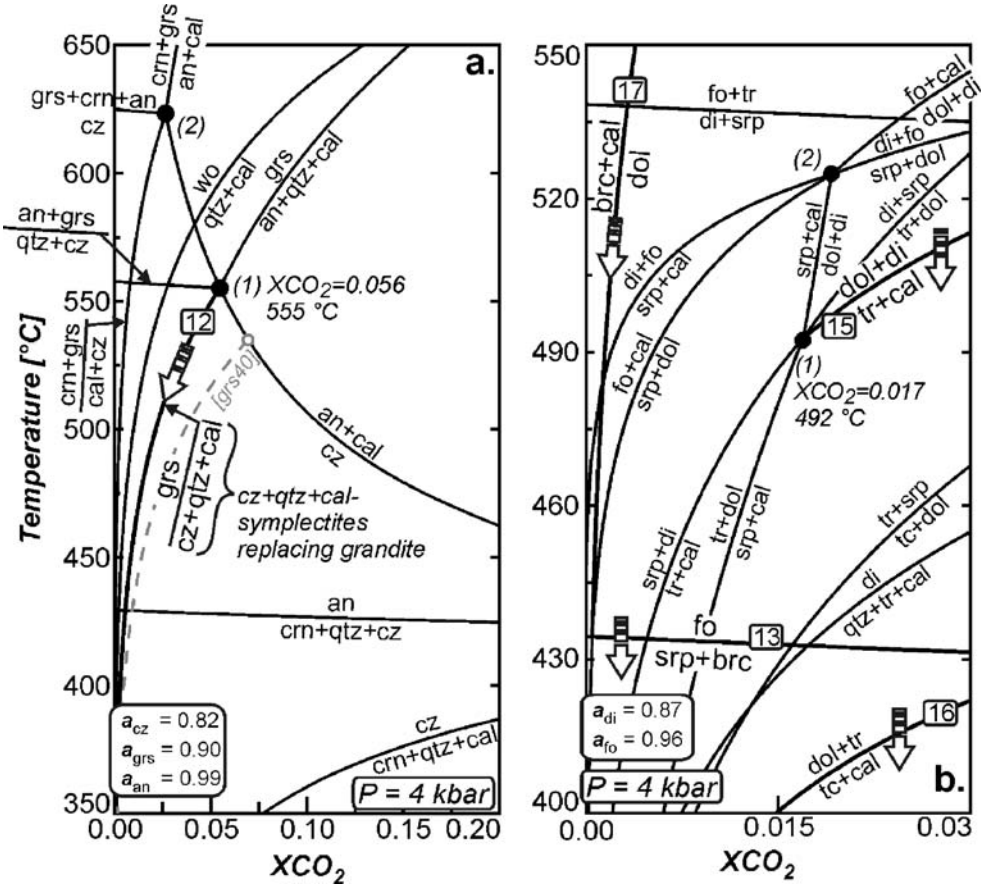

Fig. 10 **a** An isobaric T-X_{CO2} grid for the Type (1) marbles showing phase equilibria in the CASCH model system. Activity corrections were performed for clinozoisite (cz), grossular and anorthite. Reaction (12) is shown for two different grossular compositions (grey stippled line). **b** The T-X_{CO2} section for the Type (2) and (3) marbles is calculated for the system CMASCH. The reaction geometry allows derivation of a time-related retrograde reaction history. Note the low values of X_{CO2} in both diagrams

High-T phase relations in the Type (1) calc-silicate rocks

Figure 8a shows an isobaric T-a_{CO2} section at 6.5 kbar in the simplified CASC system, considering the phases: anorthite, calcite, grossular, meionite, quartz and wollastonite. Clinopyroxene is considered as an excess phase as it is present at all stages of textural development and is not included in the calculation (cf. Harley et al. 1994; Fitzsimons and Harley 1994). The phase diagram of Fig. 8a is similar to isobaric T-a_{CO2} grids described in the literature (cf. Ellis 1978; Fitzsimons and Harley 1994; Satish-Kumar and Harley 1998; Dasgupta and Pal 2005). Pseudo-invariant points are labelled with [Cal], [An] and [Wo], corresponding to the absent phase. The key constraint for minimum peak metamorphic temperatures is given by the presence of the suggested peak metamorphic mineral assemblage scapolite (a_{Me} = 0.33) + wollastonite at the pseudo-invariant point [An] where T = 853°C. Based on textural observations grandite grows at the expense of scapolite. The outer parts of grandite rims represent the original interface between scapolite and the carbonate matrix at incipient high T-retrogression, whereas the innermost parts of the grandite coronae are developed at later stages of the retrograde path. According to Joesten (1977), these grandite coronae enveloping scapolite indicate transport controlled reaction kinetics at the original scapolite-calcite phase boundary. Scapolite cores represent the original high-T composition before the onset of grandite-producing reactions (2), (3), (4), (5) and (6). For the construction of the T-a_{CO2} diagram, the lower value for the activity of grossular (a_{Grs} = 0.40, outer part of grandite rims) and the higher value for meionite activity (a_{Me} = 0.33, scapolite cores) were considered to represent the high-T metamorphic assemblage, when coronal grandite was formed during early cooling. The lower value for the activity of meionite a_{Me} = 0.22 and the higher value for the activity of grossular a_{Grs} = 0.92 represent lower-T metamorphic conditions. The effect of varying grossular and meionite compositions on the slopes of corresponding reactions is indicated by the grey stippled reaction curves in Fig. 8a and b. Patchy inhomogeneous Fe-distribution in grandite grains (Type 1 b, Fig. 2c) as well as the gradual increase of the andradite content towards the grandite rims (Type 1c, d) suggest variable fO_2 and a_{CO2} of the fluid at closely-spaced grain interfaces between the reactant phases (cf. Dasgupta and Pal 2005). Stable C-O-isotope investigations rule out any kind of fluid infiltration out of isotopic equilibrium with the host, thus the initial values of fO_2 and a_{CO2} between the reactant phases (scapolite-wollastonite-clinopyroxene) possibly control the composi-

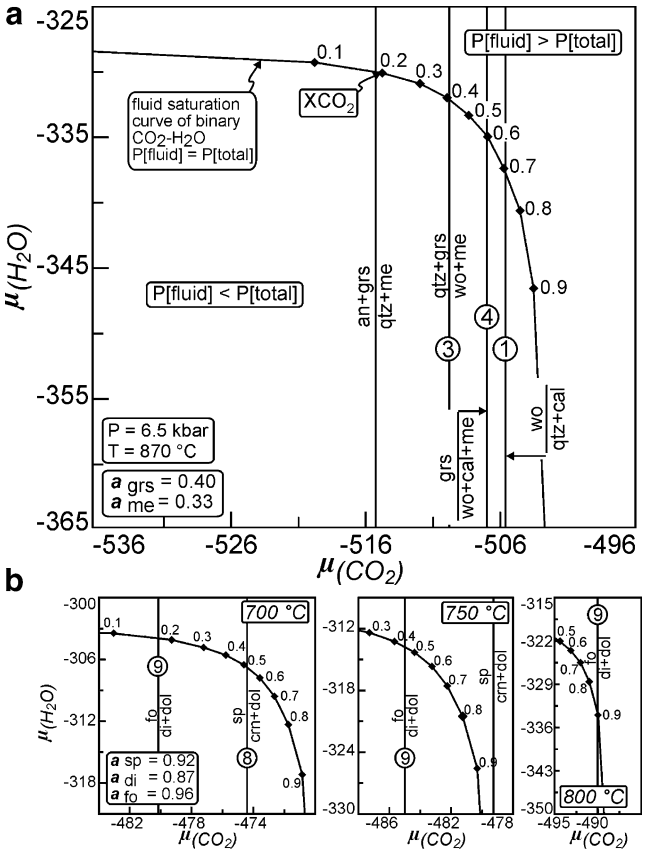

Fig. 11 μH_2O-μCO_2 diagrams. The fluid saturation curve is plotted for a binary H_2O-CO_2 fluid, where $P_{fluid} = P_{total}$. Values of X_{CO2} are given. Activity corrections were performed for grossular, meionite, spinel, diopside and forsterite. **a** Type (1) marbles are calculated in the chemical system CASCH at 6.5 kbar and 870°C; **b** The chemical system CMASCH is used for the Type (2) and (3) marbles at 6.5 kbar and 700-800°C. Phase relations are projected from calcite

tional zoning of grandite garnet, where higher values of fO_2 enhance the formation of andradite-rich grandite at high-T at the onset of cooling. The Fe^{3+}, required for andradite formation is considered to stem from the oxidation of Fe^{2+} from clinopyroxene. Grandite coronas with a_{Grs} = 0.4 developed at T>853°C, via reaction (3) and/or (4) in Fig. 8a, and equilibrated with a fluid of high to intermediate CO_2 activity. Increasing a_{Grs} from 0.5, 0.7 to 0.9 is reflected in a drop in temperature to 770°C, decreasing CO_2 activities and a lowering in fO_2. According to the study of Lamb et al. (1987), the high oxidizing conditions at the onset of cooling (a_{Grs} = 0.4) are compatible with a CO_2-dominated fluid, whereas low activities of CO_2 are typical for more reduced fO_2 conditions. The reaction geometry of the coronal grandite-forming reactions (2) and (3) in the isobaric T-a_{CO2} section (Fig. 8a) and P-a_{CO2} diagram (Fig. 8b) indicates incipient isobaric cooling and a lowering of aCO_2 after the peak of metamorphism. The slope of the garnet-forming reaction (3) in the P-a_{CO2} section (Fig. 8b) also allows an increase in P during growth of coronal garnet. The shift towards lower values of aCO_2 of the corresponding pseudo-invariant points [An] and [Cal] in Fig. 8b at lower metamorphic grade (~750°C, a_{Me} = 0.22; a_{Grs} = 0.92) suggests isobaric cooling as a driving force of the formation of coronal grandite. The breakdown of meionite via reaction (11) at low temperatures (Fig. 8a) took place after coronal garnet was formed, consistent with textural observations.

High-T phase relations in the Type (2) dolomitic marbles

To examine phase relations of the siliceous dolomitic marbles, a T-a_{CO2} section for the simplified CMASCH chemical system was calculated (Fig. 9). Calcite was treated as an excess phase and the calculation was performed at a pressure of 6.5 kbar. A sequence of decarbonation reactions characterises the chemical system of impure dolomitic marbles during prograde metamorphism. Assuming an internally buffered fluid evolution, where liberated fluids are in local equilibrium with the reactant phases in the flow system (Baumgartner and Ferry 1991; Ferry 1991), the reaction geometry in Fig. 9 allows temporal constraints to be placed on reactions (7), (8), (9) and (10). The absence of periclase and pseudomorphic brucite after periclase constrains aCO_2 to relatively high values at temperatures of ~860°C. Coronal clinopyroxene that formed at the expense of quartz and dolomite by reaction (7) (Fig. 4a), represents an early stage of metamorphism. During transient prograde metamorphism, spinel formed by reaction (8) (Fig. 4b), followed by formation of forsterite via reaction (9), (Fig. 4c) at temperatures below 790°C and high values of aCO_2. However, the reaction geometry in Fig. 9 and the lack of important (pseudo) invariant-points provide insufficient reliable evidence to constrain the P-T-fluid history. The gentle dT/d[log]a_{CO2} slope of the coronal clinopyroxene forming reaction (9) in Fig. 9 is consistent with cooling after the peak of metamorphism.

Low temperature phase relation in the Type (1), (2) and (3) marbles

For Type (1) marbles, the formation of epidote-quartz-calcite symplectites (Fig. 5a) via reaction (12) is the only significant retrograde hydration reaction, which occurs at temperatures below 550°C and low X_{CO2} values in T-X_{CO2} space (Fig. 10a). In the Type (2, 3) marbles, a more complete retrograde hydration reaction sequence is evident (Figs. 5b,c and 10b). At about 500°C, hydration of diopside produces tremolite by reaction (15) (Fig. 5b) and pseudomorphic brucite is formed after dolomite via reaction (17) under more H_2O-rich conditions (Fig. 5d). The hydration reaction forsterite = serpentine + brucite (reaction 13) is relatively insensitive to X_{CO2} and indicates temperatures

below 440°C. The latest record of cooling is the formation of talc at about 400°C by reaction (16) (Fig. 5c).

μH_2O-μCO_2 diagrams

μH_2O-μCO_2 diagrams provide a good method to evaluate whether Ptot was equal to or grater than Pfluid. Thus, equilibrium phase relations involving silicate and carbonate phases were calculated as a function of the chemical potentials of H_2O and CO_2 in μ-μ space for the system CASCH at 870°C and CMASCH for 700, 750 and 800°C, all at 6.5 kbar (Fig. 11a and b). Due to the absence of sulphur-bearing phases (e.g. pyrrhotite, pyrite), a ternary C-O-H fluid is considered. All reactions in Fig. 11a and b are decarbonation reactions, thus all have a vertical geometry.

For the Type (1) marbles (Fig. 11a) the relevant mineral forming reactions (1), (3) and (4) intersect the fluid-saturation curve at X_{CO2} of ca. 0.4, 0.6 and 0.7.

Formation of grandite coronas during early cooling by reactions (3) and (4) under fluid-saturated conditions would require a certain amount of external H_2O that is not substantiated by stable isotope data. Either these amounts were very minute, so as to not leave an isotope record, or reactions started slightly below the fluid-saturation curve with a pure CO_2 fluid at $P_{fluid} < P_{total}$ or even just under conditions of grain boundary wetting by CO_2 molecules which not yet form a proper phase in the thermodynamic sense. In such a situation diffusion is likely to be very slow and the amount of reaction progress small, as indicated by the thin corona textures. The reactions are self-limiting as the CO_2 produced impedes reaction progress, hence diffusion of CO_2 out of the system controls actual reaction progress.

The shift of the fluid saturation curve and the intersections with reaction (8) and (9) from 700 to 800°C at 6.5 kbar is shown in Fig. 11, for the Type (2) and (3) marbles. At 700°C, reaction (8) and (9) intersect with the fluid saturation curve at X_{CO2} of ~0.5 and ~0.18 respectively. At 750 and 800°C reaction (8) lies outside the fluid saturation curve, where $P_{fluid} > P_{total}$, this case is not realized in nature. Reaction (9) intersects at X_{CO2}~0.4 at 750°C and ~0.9 at 800°C. In both reactions (8) and (9) the high-T mineral assemblage lies on the low μCO_2 side, hence, their stability is enhanced at more water rich conditions. Consequently the stability of the corona forming mineral assemblage dolomite-diopside enveloping forsterite (reaction 9, Fig. 4c,d) is increased at higher values of CO_2.

Summary of the fluid evolution

The carbonate fraction $\delta^{18}O$ and $\delta^{13}C$ isotope data constrain a four-stage fluid/rock evolution (Fig. 12a,b):

(I) A pre-peak-metamorphic infiltration of externally derived fluids depleted in $\delta^{18}O$ caused a shift in primary sedimentary $\delta^{18}O$ values (~23‰) to lower values ($\delta^{18}O$ ~19.6 to 20‰).

(II) During incipient prograde metamorphism the processes of batch- and Rayleigh fractionation became more important and contributed to a coupled ^{13}C and ^{18}O depletion during decarbonation reactions. In the sense of external fluid infiltration, the Type (1) calc-silicate behaved as a closed system with minor depletion in $\delta^{13}C$. A larger depletion in $\delta^{13}C$ was attained along ductile folds in granulite-facies rocks, which are ascribed to partially open-system conditions where fluid could escape rather continuously from the reaction site. Thus, when fluid flow occurred during peak-metamorphic recrystallization, it was rather focused than pervasive.

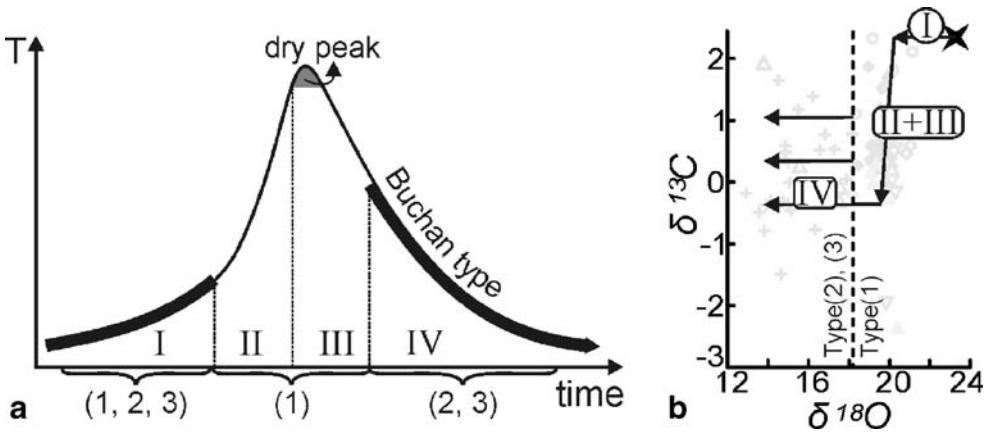

Fig. 12 **a** A time-temperature path to demonstrate the combined temperature-fluid history of the three different marble types. The geometry of the T-t curve (solid black curve) is similar to a Buchan-type metamorphism. The thick solid black curves at the beginning and the end of the T-t path indicate open system conditions, where external fluid could infiltrate the rocks. The four different stages of the time-temperature fluid history are labelled I, II, III, IV. The marble types that provide evidence for each time-temperature-fluid event are given in brackets below the time axis; **b** the four-stage fluid evolution path is shown in the $\delta^{18}O$–$\delta^{13}C$ plot (I–IV)

(III) At the metamorphic peak, H_2O-absent conditions are assumed for the Type (1) marbles. Stable isotope data for Type (1) marbles rule out any infiltration of fluid that was out of isotopic equilibrium during isobaric cooling. Low fluid pressure ($P_{fluid} < P_{rock}$; Fig. 12a, b) and heterogeneities in fO_2 produced higher values of a_{CO2} that lead to the formation of andradite-rich grandite coronae during isobaric cooling. Clinopyroxene-dolomite coronae around forsterite may have formed under similar P-T-aCO_2 conditions.

(IV) Type (2) and (3) marbles underwent post-peak-metamorphic water-rich fluid infiltration, which led to the hydration of former high-T mineral assemblages by formation of brucite, serpentine, talc or tremolitic amphibole and to the precipitation of low-Mg calcite, depleted in ^{18}O. Therefore, Type (2) and (3) marbles give no reliable evidence for the P-T-fluid conditions at the peak of metamorphism. Type (1) calc-silicate assemblages were not largely affected by retrograde hydration reactions, only grandite garnet was locally consumed to form epidote-quartz-calcite symplectites. Thus, Type (1) marble underwent fluid-absent cooling under closed-system conditions and could be used to interpret the high-T fluid-rock evolution of the La Huerta marble layers. A very limited extent of retrograde reaction in Type (1) marbles was also noted by Ernst (1990), who described substantial updip "expulsion" of volatiles attending recrystallization. Thus, only small amounts of H_2O and CO_2 were available for hydration and carbonation during uplift.

Conclusions

P-T evolution

The geodynamic setting of a regional contact metamorphic event in the La Huerta Range constrains the P-T-t fluid path close to Buchan-type metamorphic conditions, in which an advective heat source is responsible for high-T metamorphism at intermediate pressure. The studied siliceous marbles experienced peak metamorphic temperatures above ~860°C at 6.5 kbar. Based on thermodynamic modelling in the CASC system, an isobaric cooling path from T = ~860°C to T = 750°C at intermediate CO_2 activities is proposed.

Fluid evolution

A four-stage fluid evolution is proposed, with a pre-metamorphic hydration of rocks by cogenetic sediment-derived fluids and metamorphic fluids from deeper levels in the crust. Fluid-absent conditions prevailed at the metamorphic peak, and advected heat expelled any remaining fluid from the rocks. Significant hydration occurred on the cooling path when fluids infiltrated Type (2) and (3) marbles. Although the model presented above is consistent with observations, the interpretation of the stable oxygen isotope data is equivocal, since fluid-rock interaction can occur at any stage, from early burial, to the peak of metamorphism, to uplift and weathering at the Earth's surface. Thus samples strongly depleted in ^{18}O may record the passage of externally derived fluids at any point during the rock's history.

Acknowledgements We gratefully acknowledge the constructive comments of G. Hoinkes, C. A. Hauzenberger, F. Bernhardt, K. Stüwe, M. F. Gargiulo, T. Johnson and A. Proyer. A. Leis from Joanneum Research Graz and S. Muellegger from Karl-Franzens University, Graz, are thanked for oxygen and carbon isotope analyses. We thank R. Abart for the critical editorial handling of the manuscript. This study was financially supported by the Austrian Science Research fund project FWF P17350-N10 to A. Mogessie

References

Abart R (1995) Phase equilibrium and stable isotope constraints on metasomatic vein formation. Contrib Mineral Petrol 122:116–133

Abart R, Schmud R, Harlov D (2001) Metasomatic coronas around hornblendite xenoliths in granulite facies marble, Ivrea zone, N Italy, I: constraints on component mobility. Contrib Mineral Petrol 141:473–493

Abart R, Sperb R (2001) Metasomatic coronas around hornblendite xenoliths in granulite facies marble, Ivrea zone, N Italy. II: Oxygen isotope patterns. Contrib Mineral Petrol 141:494–504

Baker J, Newton RC (1995) Experimental determined activity-composition relations for Ca-rich scapolite in the system CaAl2Si2O8-NaAlSi3O8-CaCO3 at 7 kbar. Am Mineral 80:744–751

Baumgartner LP, Ferry JM (1991) A model for coupled fluid-flow and mixed-volatile mineral reactions with applications to regional metamorphism. Contrib Mineral Petrol 106:273–285

Bhowmik SK, Dasgupta S, Hoernes S, Bhattacharva PK (1995) Extremely high-temperature calcareous granulites from the Eastern Ghats, India: evidence for isobaric cooling, fluid buffering, and terminal channelized fluid flow. Eur J Mineral 7:689–703

Broecker WS, Oversby VM (1971) Chemical equilibrium in the earth. McGraw-Hill, New York

Brown PE, Bowman JR, Kelly WC (1985) Petrologic and stable isotope constraints on the source and evolution of skarn-forming fluids at Pine Creek, California. Economic Geology 80:72–95

Caminos R (1979) Sierras Pampeanas Noroccidentales. Salta, Tucumà, Catamarca, La Rioja y San Juan. In: Leanza EF (ed) II Simposio de Geología Regional Argentina 1. Academia Nacional de Ciencias, Córdoba, pp 225–291

Cartwright I, Buick IS (1995) Formation of wollastonite-bearing marbles during late regional metamorphic channelled fluid flow in the upper calc-silicate unit of the Reynolds Range Group, central Australia. J Met Geol 13:397–417

Cartwright I, Vry J, Sandiford M (1995) Changes in stable isotope ratios of metapelites and marbles during regional metamorphism,

Mount Lofty Ranges, South Australia: implications for crustal scale fluid flow. Contrib Mineral Petrol 120:292–310

Castro de Machuca B (1990) Caracterización petrológica del basamento cristalino del extremo sur de la sierra de La Huerta, San Juan, Argentina. XI Congreso Geológico Argentino, Actas I, San Juan, pp 157–161

Castro de Machuca B, Sumay BC, Pontoriero S, Conte-Grand A, Meissl E (1995) Aspectos petrológicos de las rocas máficas y ultramáficas de la sierra de La Huerta, San Juan, Argentina. Actas 6 Simposio Sul-Brasileiro de Geologia y 1 Encontro de Geologia do Cono Sul, Porto Alegre, Brasil, pp 162–167

Connolly JAD (1990) Multivariable phase-diagrams: an algorithm based on generalized thermodynamics. Am J Sci 290:666–718

Dalziel IWD, Dalla Salda LH, Gahagan LM (1994) Paleozoic Laurentia-Gondwana interaction and the origin of the Appalachian-Andean mountain system. Geol Soc Am Bulletin 106:243–252

Dasgupta S, Pal S (2005) Origin of grandite garnet in calc-silicate granulites: mineral-fluid equilibria and petrogenetic grids. J Petrol 46:1045–1076

De Bresser JHP, Spiers CJ (1997) Strength characteristics of the r, f, and c slip systems in calcite. Tectonophysics 272:1–23

Delpino S, Bjerg E, Mogessie A, Schneider I, Gallien F, Castro de Machuca B, Previley L, Meissl E, Pontoriero S, Kostadinoff J (2008) Deformation mechanisms in granulite-facies minerals, Valle Fértil Range, San Juan province, Argentina. Revista de la Asociación Geológica Argentina 63(2):21–35

Ellis DE (1978) Stability and phase equilibria of chloride and carbonate bearing scapolites at 750°C and 4000 bar. Geochim Cosmochim Acta 42:1271–1281

Ernst WG (1990) Thermobarometric and fluid expulsion history of subduction zones. Journal of Geophysical Research 95:9047–9053

Evans BW, Shaw DM, Houghton DR (1969) Scapolite stoichiometry. Contrib Mineral Petrol 24:193–305

Ferry JM (1991) Dehydration and decarbonation reactions as a record of fluid infiltration. In: Kerrick DM (ed) Contact Metamorphism. Rev Min 26:351–393

Ferry JM, Dipple GM (1992) Models for coupled fluid flow, mineral reaction and isotopic alteration during contact metamorphism: the Notch Peak aureole, Utha. Am Mineral 77:577–591

Ferry JM, Newton RC, Craig EM (2002) Experimental determination of the equilibria: rutile + magnesite = baddeleyite + forsterite + CO2. Am Mineral 87:1342–1350

Fitzsimons CW, Harley SL (1994) Garnet coronas in scapolite-wollastonite calc-silicates from East Antarctica: the application and limitations of activity-corrected grids. J Met Geol 12:761–777

Gallien F, Abart R, Wyhlidal S (2007) Contact metamorphism and selective metasomatism of the layered Bellerophon Formation in the eastern Monzoni contact aureole, northern Italy. Mineral Petrol 91:25–53

Greenwood HJ (1967) Mineral equilibria in the system MgO-SiO2-H2O-CO2. In: Abelson PH (ed) Res Geochem 2. Wiley & Sons, New York, pp 542–567

Greenwood HJ (1975) Buffering of pore fluids by metamorphic reactions. Am J Sci 275:573–593

Gregory RT, Criss RE (1986) Isotopic exchange in open and closed systems. In: Valley JW, Taylor HP Jr, O'Neil JR (ed) Stable Isotopes in high temperature geological processes. Rev Min 16:91–127

Harley SL, Buick IS (1992) Wollastonite-scapolite assemblages as indicator of granulite pressure-temperature-fluid histories: the Rauer Group, East Antarctica. J Petrol 33:693–728

Harley SL, Fitzsimons ICW, Buick IS (1994) Reactions and textures in wollastonite-scapolite granulites and their significance for pressure-temperature-fluid histories of highgrade rerranes. Precambrian Research 66:309–323

Holland TJB, Powell R (1998) An internally consistent thermodynamic data set for phases of petrological interest. J Met Geol 3:309–343

Holness MB, Graham CM (1991) Equilibrium dihedral angles in the system H2O-CO2-NaCl-calcite, and implications for fluid flow during metamorphism. Contrib Mineral Petrol 108:368–383

Joesten R (1977) Evolution of mineral assembalge zoning in diffusion metasomatism. Geochim et Cosmochim Acta 41:649–670

Lamb WM, Valley JW, Brown PE (1987) Post-metamorphic CO2-rich fluid inclusions in granulites. Contrib Mineral Petrol 96:485–495

Mathavan V, Fernando GWAR (2001) Reactions and textures in grossular-wollastonite-scapolite-calc-silicate granulites from Maligawila, Sri Lanka: evidence for high-temperature isobaric cooling in the meta-sediments of the Highland Complex. Lithos 59:217–232

Moecher DP, Valley JW, Essene EJ (1994) Extraction and carbon isotope analysis of CO2 from scapolite in deep crustal granulites and xenoliths. Geochim Cosmochim Acta 58(2):959–967

Mogessie A, Ettinger K, Leake BE (2004) AMPH-IMA04: a revised hypercard program to determine the name of an amphibole from chemical analyses according to the 2004 international mineralogical association scheme. Mineral Mag 68(5):825–830

Mogessie A, Schneider I, Gallien F, Castro de Machuca B, Bjerg EA, Delpino S, Prviley L, Pontoriero S, Meissl E, Kostadinoff J (2007) Reaction rims in gabbros and their petrological significance, Valle Fèrtil and La Huerta Ranges, San Juan province, Argentina. Mitt Öster Mineral Ges 153:83

Motoyoshi Y, Thost DE, Hensen BJ (1991) Reaction textures in calc-silicate granulites from the Bolingen Islands, Prydz Bay, East Antarctica: implications for retrograde P-T path. J Met Geol 9:293–300

Nabelek PI, Labotka TC, O'Neil JR, Papike JJ (1984) Contrasting fluid/rock interaction between Notch peak granite intrusion and argillites and limestones in western Utha: evidence from stable isotopes and phase assemblages. Contrib Mineral Petrol 86:25–34

Nabelek PI (1991) Stable isotope monitors. In Kerrick DM (ed) Contact Metamorphism. Rev Min 26:395–435

Olgaard DL, Evans B (1988) Grain growth in synthetic marbles with added mica and water. Contrib Mineral Petrol 100:246–260

Otamendi JE, Tibaldi AM, Vujovich GJ, Vinao GA (2007) Metamorphic evolution of migmatites from deep Famatinian arc crust exposed in Sierras Valle Fèrtil-La Huerta, San Juan, Argentina. J South Am Earth Sci 2007.09001.DOI 10.1016/

Pankhurst RJ, Rapela CW, Saavedra J, Baldo E, Dahlquist J, Pascua I, Fanning CM (1998) The famatinian magmatic arc in the central Sierras Pampeanas: an Early to Mid-Ordovician continental arc on the Gondwana margin. Geol Soc London, Special Publications 1998 142:343–367

Pankhurst RJ, Rapela CW, Fanning CM (2000) Age and origin of coeval TTG, I- and S-type granites in the Famatinian belt of NW Argentina. Transaction Royal Society Edinburgh. Earth Sciences 91:151–168

Pontoriero S, Castro de Machuca B (1999) Contribution to the age of the igneous-metamorphic basement of the La Huerta Range, Province of San Juan, Argentina. Actas II South American Symposium on Isotope Geology, Argentina, Córdoba, pp 101–104

Povoden E, Horacek M, Abart R (2002) Contact metamorphism of siliceous dolomite and impure limstones from the Werfen formation in the eastern Monzoni contact aureole. Mineral Petrol 76:99–120

Ragona D, Anselmi G, González P, Vujovich G (1995) Mapa geológico de la Provincia de San Juan. Escala 1:500.000. SEGEMAR, Buenos Aires

Ramos VA, Vujovich GI, Dallmeyer RD (1996) Los klippes y ventanas tectónicas de la estructura preándica de la Sierra de Pie de Palo (San Juan): edad e implicanciones tectónicas. Actas XIII Congreso Geológico Argentino y III Congreso de Exploración de Hidrocarburos 5:377–392

Rapela CW, Coira B, Toselli A, Saavedra J (1992) El magmatismo del Paleozoico inferior en el Sudeste de Gondwana. In: Gutierrez MJ, Saavedra J, Rabano J (eds) Paleozoico inferior de Ibero-America. Universidad de Extremadura, Spain, pp 21–68

Rosenbaum JM (1994) Stable isotope fractionation between carbon dioxide and calcite at 900°C. Geochim Cosmochim Acta 58 (17):3747–3753

Rossi JN, Toselli AJ, Saavedra J, Sial AN, Pellitero E, Ferreira VP (2002) Common crustal source for contrasting peraluminous facies in the Early Paleozoic Capillitas Batholith, NW Argentina. Gondwana Res 5:325–337

Rumble D (1982) Stable isotope fractionation during metamorphic volatilization reactions. In: Ferry JM (ed) Characterization of metamorphism through mineral equilibria. Rev Min 10:327–353

Saavedra J, Toselli A, Rossi J, Pellitero E, Durand F (1998) The early palaeozoic magmatic record of the famatina System: a review. In: Pankhurst RJ, Rapela CW (eds) Special PublicationGeological Society London The Prot-Andean Margin of Gondwana, 142:283–295

Satish-Kumar M, Harley SM (1998) Reaction textures in scapolite-wollastonite-grossular calc-silicate rock from the Kerala Khondalite Belt, Southern India: evidence for high-temperature metamorphism and initial cooling. Lithos 44:83–99

Schenk V (1983) Petrology of felsic granulites, metapelites, metabasics, ultramafics, and metacarbonates from Southern Calabria (Italy): prograde metamorphism, uplift and cooling of a former lower crust. J Petrol 25:255–298

Schneider I, Mogessie A, Gallien F, Castro de Machuca B, Bjerg E, Delpino S, Previley L, Pontiero S, Meissl E, Kostadinoff J (2006) Coronitic gabbros and associated basement rocks of the Valle Fèrtil- La Huerta Range, San Juan Province, NW Argentina. Conference Series, Pangeo Austria 2006; Innsbruck University press, p 316

Sengupta P, Sanyal S, Dasgupta S, Fukuoka M, Ehl J, Pal S (1997) Controls of mineral reactions in high-grade garnet-wollastonite-scapolite-bearing calc-silicate rocks: an example from Anakapalle Eastern Ghats, India. J Met Geol 15:551–564

Shaw DM (1960) The geochemistry of scapolite: I. Previous work and general mineralogy. J Petrol 1:218–260

Shaw RK, Arima M (1996) High-temperature metamorphic imprint on calc-silicate granulites of Rayagada, Eastern Ghats, India: implication for the isobaric cooling path. Contrib Mineral Petrol 126:169–180

Shieh YN, Taylor HP (1969) Oxygen and hydrogen isotope studies of contact metamorphism in the Santa Rosa range, Nevada, and other areas. Contrib Mineral Petrol 20:306–356

Taylor HP, Sheppard SMF (1986) Igneous rocks: I. Processes of isotopic fractionation and isotope systematic. In: Valley JW, Taylor HP Jr, O'Neil JR (ed) Stable isotopes in high temperatures geological processes. Rev Min 16:227–271

Thomas WA, Astini RA (1996) The Argentine Precordillera: A traveler from the Ouachita embayment of North American Laurentia. Science 273:752–757

Thompson AB, Connolly JAD (1992) Migration of metamorphic fluid: some aspects of mass and heat transfer. Earth Sci Rev 32:107–121

Toselli AJ, Durand FR, Rossi de Toselli JN, Saavedra J (1996) Esquema de evolución geotectónica y magmática Eopaleozoica del sistema de Famatina y sectores de Sierras Pampeanas. Actas XIII Congreso Geológico Argentino y III Congreso de Exploración de Hidrocarburos 5:443–462

Valley JW (1986) Stable isotope geochemistry of metamorphic rocks. In Valley JW, Taylor HP Jr, O'Neil JR (ed) Stable isotopes in high temperatures geological processes. Rev Min 16:445–489

Valley JW, O'Neil JR (1981) 13C/12C exchange between calcite and graphite: a possible thermometer in Grenville marbles. Geochim Cosmochim Acta 45:411–419

Veizer J, Hoefs J, Low DR, Thurston PC (1989) Geochemistry of Precambrian carbonates: II. Archean greenstone belts and achean sea water. Geochim Cosmochim Acta 53:859–871

Vry JP, Brown E, Valley JW, Morrison J (1988) Constraints on granulite genesis from carbon isotope compositions of cordierite and graphite. Nature 332:66–68

Vujovich G, Pleters P, Tchilinguirian P, Chernikoff J, Lyons P, Stuart-Smith P, Marin G, Turel A, Skirrow R, López H (2000) Carta geologica de la Rebublica Argentina, Chepes 3166-III, Programa Nacional de Cartas Geologicas Ley N. 24.224 de Reordenamiento Minero.

Warren RG, Hensen BJ, Ryburn RJ (1987) Wollastonite and scapolite in Precambrian calc-silicate granulites from Australia and Antarctica. J Met Geol 5:213–233

Zheng JF (1994) Oxygen isotope fractionation in metal monoxides. Mineral Mag 58A:1000–1001